Ministerul Educației Naționale
Universitatea POLITEHNICA din București
Școala Doctorală de Inginerie Industrială și Robotică

Decizie Senat UPB nr.864 / 28.06.2022

Phd Thesis
Abstract

The integrated concept of an innovative linear axis specific to lightweight construction machine

Author: Ing. Sorin-Alexandru BURDUCEA
Coordonator: Prof. univ. Dr. Ing. Miron ZAPCIU

Doctoral committee

Președinte	Prof. univ. dr. ing. Nicolae IONESCU	Universitatea POLITEHNICA din București
Conducător de doctorat	Prof. univ. dr. ing. Miron ZAPCIU	Universitatea POLITEHNICA din București
Membri	Prof. univ. dr. ing. Tudor-Ion DEACONESCU	Universitatea TRANSILVANIA din Brașov
	Prof. univ. dr. ing. Mihăiță HORODINCĂ	Universitatea tehnică "Gheorghe Asachi" din Iași
	Prof. univ. dr. ing. Costel-Emil COTEȚ	Universitatea POLITEHNICA din București

Table of Contents

Introduction

„75% of all businesses fail, and one of the top 5 causes is lack of flexibility," Investopedia, January 10, 2022 - based on data from the Bureau of Labor Statistics, USA.

a. Research motivation

The desire of every customer is to have access to products designed specifically for their desires and needs. Each individual has their own preferences and wants to express their individuality in their own unique way. When it comes to furniture products, they not only bring utility and comfort but also shape the environment we live in. It has always been a key element of our well-being, promoting our lifestyle, similar to how clothing does, for example. Customized clothing is commonplace, but when it comes to furniture, things are completely different. Furniture manufacturing factories have dozens of employees and traditional production machines, which are efficient when following a predetermined and rigid production plan. The result of this process is mass production, which, although cost-effective, does not provide a satisfactory level of customization.

Flexibility is the main asset of the new industrial revolution, and by utilizing the concepts, ideas, and processes proposed by it, a restructuring of the production environment can be achieved to such a level that mass production of customized products becomes possible. The change requires not only the introduction of state-of-the-art information technology systems but also a new generation of production machines. These machines need to be as flexible, open, innovative, mobile, transparent, coherent, and powerful as the information itself. Literature in this direction is very scarce. The focus is almost entirely on the introduction and implementation of informational technologies and hardly at all on the actual production side. There is even the idea that the current industrial revolution is based on traditional machines. There is a gap in the literature, particularly regarding the ways in which production machines need to change with the advancement of IT control systems and the immense importance these changes have on the business level. By analyzing production processes, machines, and directly linking them to customer behavior, this work harnesses the benefits of using an ultra-flexible production system:

Mobile, meaning without a fixed location - produce everything exactly where it is needed using a local supply chain, reducing transportation costs and delivery time; an additional advantage would be offering a more environmentally friendly footprint.
Ultra-portable - ultra-small and lightweight footprint, allowing it to be easily transported in trucks to customer locations.
Fully automated and atomistic - the machine is essentially a miniaturized factory capable of delivering all production processes in a single package.
Black box - the user does not need to know the processes performed by the machine in order to successfully operate it and produce goods.
Delivers unique goods in each cycle - each complete cycle of the machine can be entirely different from the previous or next one, without mechanical changes or reprogramming of the machine, empowering mass production of customized products.
Scalable - easy parallelization of machines, allowing scalability from a single machine to thousands.
Grows with the business - to increase production, you only need to add and parallelize more machines; you can start with a small investment and invest more as your business volume grows.
Production as a service - the ability to gather machines in "farms," as described by the "production as a service" paradigm ([1]).
Reduced cost and lifespan (short-cycle machine) - by reducing the machine's lifespan from the usual twenty years to just five years,

a tenfold reduction in the machine's price can be achieved.

Quick return on investment - a long-lifespan machine is costly and may not reach its expected lifespan primarily due to moral depreciation. A machine that proposes low acquisition costs, with a lifespan of only five years, and high production rates will pay for itself in a few months, require minimal investments, and allow the factory to easily keep up with new technologies every five years.

Promotion of cooperation - the system can be used under a cooperation platform to connect production sites with designers and consumers.

Freedom to use the most optimal business model ([2]):

Classic factory - fixed location, in-house design team.

Farms - design anywhere, produce anywhere: distributed locations and production as a service; design teams can be accessed through a cooperation platform; design teams access production sites closest to the client or those with unused capacity.

Mobile - produce at the customer's location, with the local supply chain; empowers the business to expand beyond local and national borders, reaching an exponentially larger customer base.

Rental - borrow production capacities by borrowing one or more machines.

The purpose of this work is to study the feasibility of creating an ultra-flexible machine for the wood industry that meets the requirements mentioned above, particularly in terms of miniaturization and reduced cost and weight, through the introduction of a suite of mechanical and electrical solutions to support it. Considering that the machine is primarily built from an arrangement of over 60 axes, the research focus is directed towards finding solutions at this level.

b. Objectives

The present work presents the design of a high-precision and durable linear axis developed to meet the requirements of a flexible production system as announced in the previous chapter.

The research is focused on the stringent cost reduction associated with both the product itself and the production system it is based on. The capacity of the linear axis to be used within a modern concept of a production machine developed along the guidelines of Industry 4.0 is investigated. It should be capable of operating in highly contaminated environments with fine wood powders, which are inherent in the furniture industry.

In order to achieve the goal of reducing the acquisition cost of the production system it will be part of, the final cost of the axis needs to be 10 times lower than the average cost of currently available axes on the market. To meet the mobility requirements of the machine it belongs to, it needs to be 5 times lighter.

The research significantly utilizes advanced CAD/CAE software tools such as Siemens NX/Nastran and ANSYS AEDT, Maxwell, SIWave, HFSS, IcePak, Nexxim. In the initial phase, the constituent elements of the problem are detailed, and a preliminary study of the solution is developed, followed by a detailed analysis of the electrical and mechanical systems.

The electronic part of the axis consists of a servo system designed for actuating the linear axis. It provides precise control over the linear motion, requiring a motor to be controlled in a very precise manner. The aim of the research and development of the electrical system is to identify a hardware solution that can accommodate the firmware control of ODrive servo motors. The hardware platform will receive motion commands through a real-time pulse train interface and control the movement of brushless DC motors.

Within this work, in addition to researching new solutions in the field of linear technology, the vibration damping domain is also addressed in an attempt to propose a unified concept capable of addressing a wide range of applications such as production machines, 3D printers, pick-and-place machines, Cartesian robots, machine tools, etc. The solutions under investigation are reviewed in Chapter I, Subsection 2, and among them, due to the

small volume of the device compared to its vibration damping capacity and the scalability of the solution in terms of generating functionally similar solutions with or without external energy input (passive, semi-active, and active), the choice leaned towards researching systems based on the action of thin fluid layers constrained between two planes, or as they are referred to in the literature, "Squeezed-Film" systems.

These systems are based on the flow of a fluid compressed between two parallel plates, which propagates radially through flow. The flows generated by this process are inherently transient and non-uniform due to changes in geometry. In this thesis, the theory of thin film flows is employed to investigate how it is possible to utilize the losses caused by friction between the fluid layers, through the oscillatory compression and decompression of a fluid with a given viscosity, to achieve efficient damping of the relative motion between the compression planes.

The validation of the research will be carried out after the construction of a series of prototypes, whose static and dynamic performances will be determined by interpreting the experimental results and comparing them with conventional translation axes. The research will be able to identify to what extent the new concept is capable of replacing current technical solutions.

Chapter 1 – Developments up-to-date

Domain of linear technology is a vast one, encompassing all solutions and approaches used in the industrial field. As a fundamental element of the kinematic structure present in production machines, depending on their final destination, several major groups can be identified:

Main linear guides of machine tools: these are subjected to high dynamic loads and need to perform with micrometric precision under the influence of various cyclic disturbances caused by machining processes. The requirements include high rigidity, thermal stability, accuracy, and long lifespan. Moreover, the guides must prevent debris from entering sensitive areas. Over time, various solutions have been recognized, including but not limited to linear guides with sliding bearings, hydrodynamic bearings, hydrostatic bearings, and linear guides with rolling bearings. The most popular solutions are those based on sliding bearings and rolling bearings. In the case of the former, maximum speeds and accelerations are strongly limited, while vibration damping is excellent due to the large contact surface, friction, and the effect of lubricant film squeezing. In the case of the latter, high speeds and accelerations can be easily achieved, but vibration damping in the bearings is minimal due to low friction and the absence of the lubricant film effect. Recent research aims to combine the advantages of these two types of bearings, namely the high vibration damping capability of sliding bearings with the ease of assembly and maintenance, minimal friction, and excellent rigidity of rolling bearings. Another area of research comprises new ranges of solutions based on electromagnetic principles.

Linear guides of production machines other than machine tools: the main requirement here is resistance to corrosion from various chemical agents present in the technological processes they serve, as well as a large number of operating cycles without the need for adjustments and maintenance, along with a low cost if possible. There is a wide range of implementations in this field, and the large application area is accompanied by a diverse spectrum of solutions, mostly based either on linear units with simple sliding bearings using polymer compounds or linear units with rolling bearings. The technological advancement of complex organic compounds in recent years has resulted in the unprecedented development of polymers and composite materials incorporating polymeric materials. As a result, endurance, friction coefficients, creep, water absorption, maximum operating temperature, and other important parameters have been optimized, leading to outstanding performance. Of

particular interest is the behavior of these bearings under dry running conditions, which is specific to the wood, food, and pharmaceutical industries. Recently, the linear technology market has witnessed the emergence of composite materials that meet the highest standards in the pharmaceutical and food industries. Enhanced materials are based on thermopolymers such as ultra-high-density polyethylene, polytetrafluoroethylene, homopolymeric polyoxymethylene, polyamide, and polyetheretherketone. The composite materials include synthetic fibers such as carbon fiber, Kevlar, fiberglass, and epoxy resins.

In the optical industry and in applications where displacements are small but require sub-micrometric precision, recent research has highlighted the usefulness of employing flexible elements that generate precise rectilinear motion through deformation. This approach brings significant benefits in addition to those already mentioned, such as excellent lifespan, maintenance-free operation, reduced mechanical complexity, and absence of play.

Chapter 2 - Designing an Economical Linear Guide while Meeting Precision Requirements

2.1 Introduction

Linear guides are ubiquitous in production systems. Each application has its own specificity and requires its own approach. In the case of the wood and furniture industry in particular, the guides must withstand exposure to fine dust particles and wood powders. These powders become difficult to manage when combined with the lubricating liquids of the bearings. The combination of these two elements results in a highly viscous and abrasive material that hinders the proper functioning of the guide and significantly shortens its lifespan. Therefore, bearings that do not require lubrication are preferred. The most commonly used solutions are based on

sliding bearing technology. Among these, the best results are achieved through the use of polymer/metal material pairs. The polymers successfully used include PTFE (Teflon), POM (acetal), Polyamide (nylon), UHMWPE (ultra-high molecular weight polyethylene), while for metals, steel and aluminum are used.

This paper proposes a new and different approach in that the bearings used are not linear but rotational, and the motion is based not on sliding bearing technology but on the flexing of blades. Bearings of this type are called "compliant bearings" and are a relatively new development in the scientific landscape, making their debut in the early 2000s with the work of professors Larry Howell [3] and Jonathan Hopkins [4].

2.2 Methodology

The proposed system will be statically analyzed by determining the parameters and processes that contribute to the deformation of the system under the action of time-invariant forces. It will also be kinematically analyzed by determining the geometric parameters that influence the motion of the assembly, and dynamically analyzed by studying vibrations and moments of inertia. The values will be determined through theoretical calculations in idealized situations to streamline the calculations, and finite element analysis will be performed using the CAE Nastran platform.

2.3 Requirements

The minimum requirements for the linear guide are described below:

- Active length: >= 350mm
- Operating hours: >= 40,000 hours (5 years)
- Easy to manufacture: Less than 10 manufacturing processes
- Ability to operate in heavily polluted environments with wood powders and dust
- Maintenance-free throughout the entire lifespan: 5 years
- Lightweight: < 5000g
- Maximum error at a length of 350mm: +/- 25um
- Medium rigidity: 1N/µm

2.4 Solution draft

The schematic diagram is presented in the figure below. The solution utilizes two diametrically opposed arm structures, which generate a two-degree-of-freedom motion. The arms are inclined relative to the horizontal plane, eliminating one degree of freedom and thus producing linear motion. By extrapolating the structure, two parallelogram portions can be identified. The system can be seen as a variation of a pantograph (Figure 2.1).
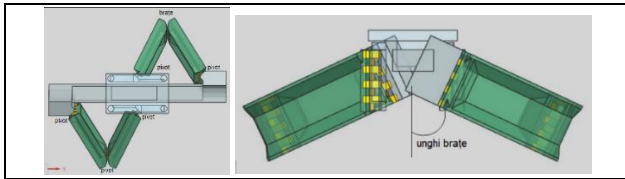
Figură 2.1 Schița sistem liniar

2.5 Kinematics

From a kinematic perspective, the system consists of two diametrically opposed arms, each generating a two-degree-of-freedom motion. By inclining the arms relative to the horizontal plane, the motion planes generated by the arms intersect, eliminating one degree of freedom and thus generating linear motion. The calculation of degrees of freedom using the Gruebler-Kutzbach mobility criterion [5] is as follows:

$$M = 6(N - 1) - 5f1 - 4f2 - 3f3 - 2f4 - f5 \quad (2.1)$$

Where:

M - the number of degrees of freedom;N - the number of kinematic pairs;f1 - the number of kinematic pairs that allow one degree of freedom (rotation or translation);f2 - the number of kinematic pairs that allow two degrees of freedom (movement in a plane or a rotation and a translation, etc.);f3 - the number of kinematic pairs that allow three degrees of freedom (movement in a plane and a rotation, 3 rotations, etc.);f4 - the number of kinematic pairs that allow four degrees of freedom (one translation and three rotations, etc.);f5 - the number of kinematic pairs that allow five degrees of freedom (three rotations and two translations, three translations and two rotations, etc.); For an arm, the degrees of freedom can be determined.

$$M = 6 * (3 - 1) - 5 * 2 = 12 - 10 = 2 \quad (2.2)$$

By intersecting the planes of the two arms (Figure 2.2), a system with a single degree of freedom along the common axis is generated. The plane A-B is generated by the arm with segments A and B, while the plane A'-B' is similarly determined by segments A' and B'.
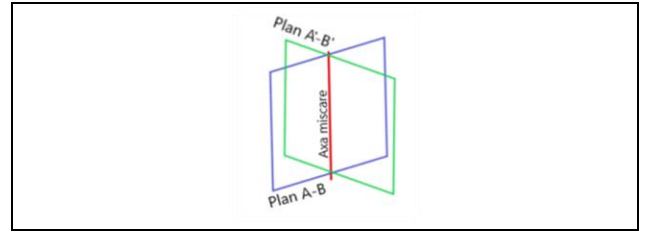
Figură 2.2 Intersecția planurilor de mișcare ale celor două brațe
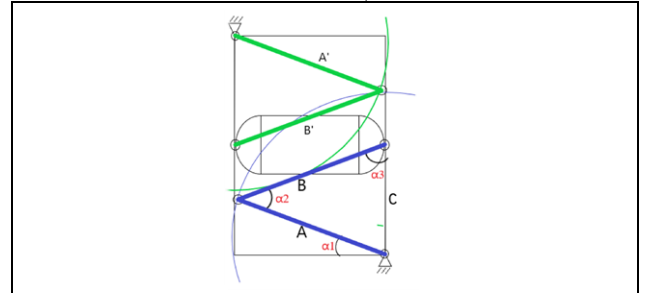
Figură 2.3 Schiță sistem cinematic

The questions we want to find answers to are: What is the best relationship between the lengths A and B? What lengths are optimal for A and B? What is the relationship between the stroke length C and the angles α1, α2, and α3? By identifying the geometric relationships in the triangle formed by the arms of the system, we can use the cosine theorem to find the solutions.:

$$C^2 = A^2 + B^2 - 2AB\cos(\alpha2) \quad (2.3)$$
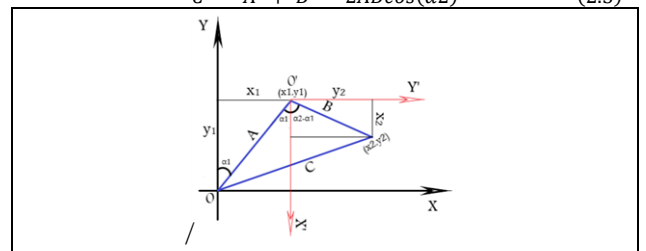
Figură 2.4 Geometria generalizată a unui braț

The values x1, y1 in the main coordinate system XOY:

$$x1 = A\sin(\alpha1) \quad (2.4)$$
$$y1 = A\cos(\alpha1) \quad (2.5)$$

The values x2, y2 in the secondary coordinate system X'O'Y'::

$$x2 = B\cos(\alpha2 - \alpha1) \quad (2.6)$$
$$y2 = B\sin(\alpha2 - \alpha1) \quad (2.7)$$

The values x2, y2 in the main coordinate system XOY, denoted as x and y:

$$x = x1 + y2 \quad (2.8)$$
$$x = A\sin(\alpha1) + B\sin(\alpha2) \quad (2.8)$$

$$y = y1 - x2 \tag{2.9}$$
$$y = A\cos(\alpha1) - B\cos(\alpha2 - \alpha1) \tag{2.10}$$

Considering the condition that side C is horizontal along the X-axis.:

$$y = 0 \tag{2.11}$$
$$A\cos(\alpha1) - B\cos(\alpha2 - \alpha1) = 0 \tag{2.12}$$

we can deduce the relationship between A, B, α1 și α2:
$$A\cos(\alpha1) = B\cos(\alpha2 - \alpha1) \tag{2.13}$$
$$C(A,B) = \sqrt{A^2 + B^2 - 2AB\cos(\alpha2)} \tag{2.14}$$

Case 1, A<B. A=U/2, iar B=U.
A + B = U/2+U=3U/2=ct.: (2.15)

$$C\left(\frac{U}{2}, U, \alpha2\right) = \sqrt{\frac{U^2}{4} + U^2 - 2U\frac{U}{2}\cos(\alpha2)} \tag{2.16}$$

$$C\left(\frac{U}{2}, U, \alpha2\right) = \sqrt{\frac{5U^2}{4} - U^2\cos(\alpha2)} \tag{2.17}$$

$$\frac{U}{2}\cos(\alpha1) = U\cos(\alpha2 - \alpha1) \tag{2.18}$$

$$\frac{1}{2}\cos(\alpha1) = \cos(\alpha2 - \alpha1) \tag{2.19}$$

Knowing that angle α1 can have values between 0 and π/2, with minimum extension at 0:

$$\frac{1}{2}\cos(0) = \cos(\alpha2) \tag{2.20}$$

$$\frac{1}{2} = \cos(\alpha2) \tag{2.21}$$

$$\alpha2 = \pm\frac{\pi}{3} \tag{2.22}$$
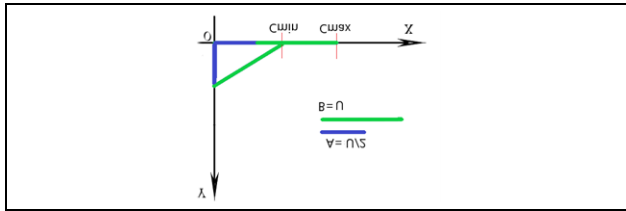
Figură 2.5 Cazul 1 A<B

Since the maximum extension for α2 is π and the solution is α2 = π/3, the value of C is given by:

$$C = Cmax - Cmin \tag{2.23}$$

$$Cmax = C\left(\frac{U}{2}, U, \pi\right) = \sqrt{\frac{5U^2}{4} - U^2\cos(\pi)} = \sqrt{\frac{9}{4}U^2} = \frac{3}{2}U \tag{2.24}$$

$$Cmin = C\left(\frac{U}{2}, U, \frac{\pi}{3}\right) = \sqrt{\frac{5U^2}{4} - U^2\cos\left(\frac{\pi}{3}\right)} = \sqrt{\frac{3}{4}U^2} = \frac{\sqrt{3}}{2}U \tag{2.25}$$

$$C = \frac{3}{2}U - \frac{\sqrt{3}}{2}U \cong 1.27U \tag{2.26}$$

Cazul 2, A>B. A=U, iar B=U/2.
$$A + B = U+U/2=3U/2=ct.: \tag{2.27}$$

$$C\left(U, \frac{U}{2}, \alpha2\right) = \sqrt{U^2 + \frac{U^2}{4} - 2\frac{U}{2}U\cos(\alpha2)} \tag{2.28}$$

$$C\left(U, \frac{U}{2}, \alpha2\right) = \sqrt{\frac{5U^2}{4} - U^2\cos(\alpha2)} \tag{2.29}$$

$$U\cos(\alpha1) = \frac{U}{2}\cos(\alpha2 - \alpha1) \tag{2.30}$$

$$\cos(\alpha1) = \frac{1}{2}\cos(\alpha2 - \alpha1) \tag{2.31}$$

In this case, if angle α1 cannot take the value of 0 because side A is greater than side B, and equation (2.13) cannot be satisfied.:

$$A\cos(0) = B\cos(\alpha2) \tag{2.32}$$
$$U = \frac{U}{2}\cos(\alpha2) \tag{2.33}$$
$$1 = \frac{1}{2}\cos(\alpha2) \tag{2.34}$$
$$2 = \cos(\alpha2)\,; imposibil\ pentru\ orice\ unghi\ \alpha2 \tag{2.35}$$

If triangle ABC can be right-angled, with a right angle at ∢ACB, then side B can fold beneath side A, and the minimum length Cmin will be A-B. Let's check if triangle ABC can be right-angled for the given case A=U/2 and B=U:

$$C^2 = A^2 + B^2 \tag{2.36}$$
$$C^2 = \frac{U^2}{4} + U^2 \tag{2.37}$$
$$C = \frac{\sqrt{5}}{2}U \tag{2.38}$$

The equations above demonstrate that there can exist a right-angled triangle ABC with a right angle at ∢ACB, and thus Cmin can be.

$$Cmin = A - B \tag{2.39}$$
$$Cmin = U - \frac{U}{2} = \frac{1}{2}U \tag{2.40}$$
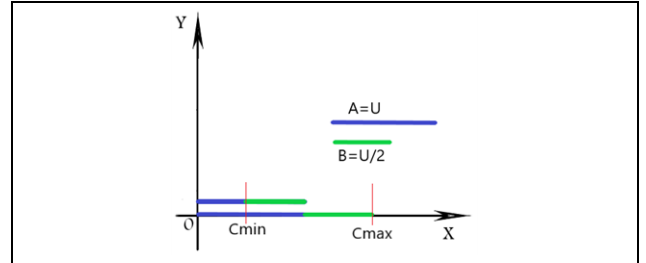
Figură 2.6 Cazul 2 A<B

$$C = Cmax - Cmin \tag{2.41}$$

$$Cmax = C\left(\frac{U}{2}, U, \pi\right) = \sqrt{\frac{5U^2}{4} - U^2\cos(\pi)} = \sqrt{\frac{9}{4}U^2} = \frac{3}{2}U \tag{2.43}$$

$$C = \frac{3}{2}U - \frac{1}{2}U = U \tag{2.44}$$

Cazul 3, A=B. A=3U/4, iar B=3U/4.
A + B = 3U/4+3U/4=3U/2=ct.:

$$C\left(\frac{3}{4}U, \frac{3}{4}U, \alpha2\right) = \sqrt{\frac{9}{16}U^2 + \frac{9}{16}U^2 - 2\frac{9}{16}U^2\cos(\alpha2)} \tag{2.45}$$

$$C\left(\frac{3}{4}U, \frac{3}{4}U, \alpha2\right) = \sqrt{\frac{18U^2}{16}(1 - \cos(\alpha2))} \tag{2.46}$$

$$C\left(\frac{3}{4}U, \frac{3}{4}U, \alpha2\right) = \frac{3}{4}U\sqrt{2(1 - \cos(\alpha2))} \tag{2.47}$$

To determine C, let's consider the minimum and maximum values of angle α2. The maximum value for α2 is π when α1 is π/2, and the arms form a straight line with

maximum extension, as in the previous cases. The minimum value that α2 can have is 0 degrees, thus:

$$C = Cmax - Cmin \qquad (2.48)$$
$$Cmax = \frac{3}{2}U \qquad (2.49)$$
$$Cmin = 0 \qquad (2.50)$$

$$C = \frac{3}{2}U \qquad (2.51)$$

Comparing the three cases, we have:

$$\text{Case 1}: C = 1.27U \ ; Caz2: C = 1.12U \ ; Caz3: C = 1.5U \qquad (2.52)$$

The case with the greatest extension of the arm is case 3, where

$$A = B \qquad (2.53)T$$

The condition is satisfied for:

$$Acos(\alpha 1) = Bcos(\alpha 2 - \alpha 1) \qquad (2.54)$$
$$cos(\alpha 1) = cos(\alpha 2 - \alpha 1) \qquad (2.55)$$
$$\alpha 1 = \alpha 2 - \alpha 1 \qquad (2.56)$$
$$\alpha 2 = 2\alpha \qquad (2.57)$$

Following the study, the most optimal relationships have been identified between the lengths of the arm segments A and B, as well as the relationship between the angles α1 and α2 in order to maximize the stroke of the axis..

2.6 Static

To achieve the desired technical requirements of the axis, it is important to determine the constructive parameters involved in defining its performance. The stiffness of the system depends on the ability of the structural elements to support loads without exceeding the maximum elastic deformations imposed. To determine these parameters using theoretical calculation methods, we will consider the arms to have a rectangular cross-section that remains constant along their length. Additionally, we will assume a homogeneous material with constant rigidity throughout its length. This approach allows us to view the system from an idealized perspective and can be determined using commonly used theoretical calculation formulas. It also enables us to identify the parameters that have the greatest impact on minimizing deformations. In the second step, we can then develop a more optimal and complex structure in terms of geometry and dimensions, which can be modeled and analyzed using finite element analysis methods..
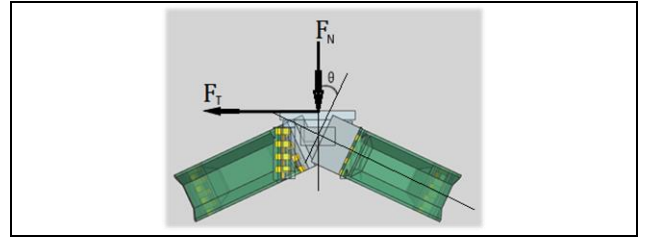
Figură 2.7 Schița încărcării pe direcție normala și tangențială
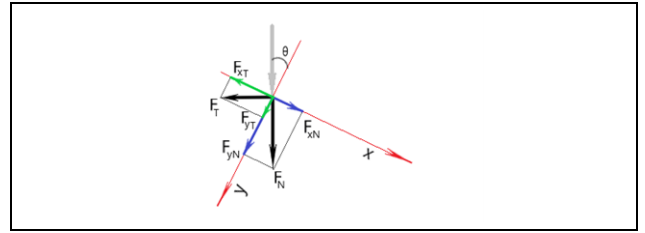
Figură 2.8 Forțele normală și tangențială descompuse în sistemul de axe al brațelor

The study of the normal force FyN derived from the force FN and the force FyT derived from FT, acting on arms A and B, is indicated graphically in Figure 2.9.
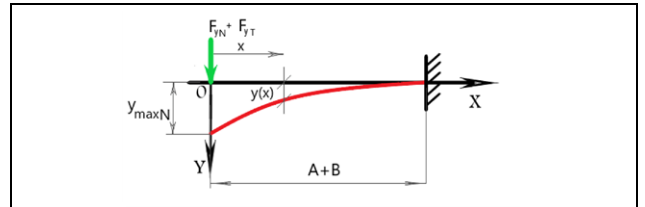
Figură 2.9 Grinda încastrată la un capăt și încărcată cu o forțele normale FyN și FyT

According to [6]-chap.11, the deformation ymax is:

$$ymaxN = \frac{(Fy_N + Fy_{NT})(A + B)^3}{3EI} \qquad (2.58)$$

Similarly to the previous case, the parameters that contribute to the deformation of the arms in the tangential direction can be determined.:
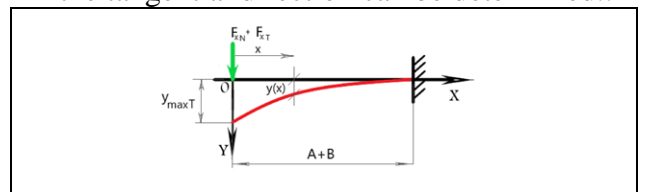
Figură 2.10 Grinda încastrată la un capăt și încărcată cu forțele tangențiale FxN și FxT

$$ymaxT = \frac{(Fx_N + Fx_{NT})(A + B)^3}{3EI} \qquad (2.59)$$

Where:

FyN, FyT, FxN, FxT are the deforming forces
A, B - are the lengths of the arm segments
EI - the stiffness of the beam expressed by E - the longitudinal modulus of elasticity (due to the ideal conditions considered and small deformations, it can be assumed to be equal to the Young's modulus) and I - the axial moment of inertia of the beam section.

In Figure 2.11, the system subjected to FEM analysis and the applied discretization are represented..
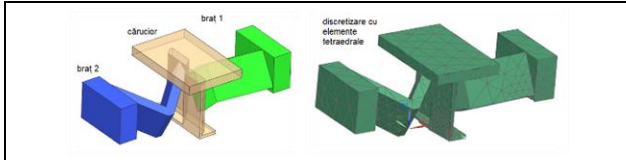
Figură 2.11 Sistem supus analizei FEM, cu și fără discretizare
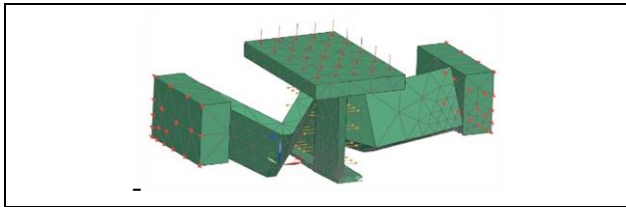
Figură 2.12 Analiza FEM - condiții la limită

The FEM solution is presented in Figure 2.13.
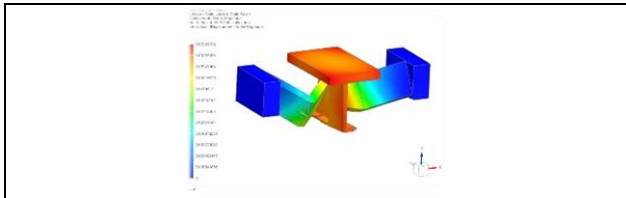
Figură 2.13 Soluția FEM - încărcare statica normala 250N

The boundary conditions in the second case, as shown in Figure 2.14, are: clamping at the edges and applying a tangential load of 100N on the surface of the moving cart..
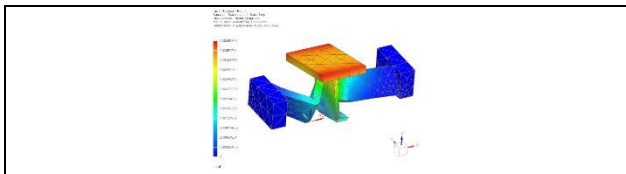
Figură 2.14 Soluția FEM - încărcare statică tangențială 100N

2.7 System dynamic

8The analytical calculation starts from an idealized system, based on the dynamic behavior of a bar with uniform cross-section and density, fixed at both ends. This model represents a geometric abstraction of the axis

and allows for the direct determination of the first two modes of vibration.
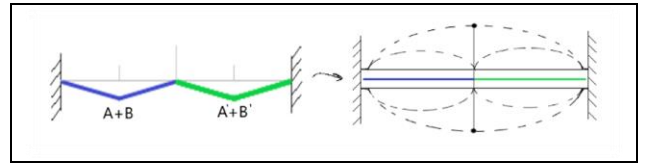
Figură 2.15 Idealizarea structurii geometrice pentru calculul modal

The idealized model analyzes the axis from the perspective of a single degree of freedom, taking into account linear characteristics for the elastic and damping forces, as shown in Figure 2.15. This model is primarily known by its Anglo-Saxon origin name: "lumped model."
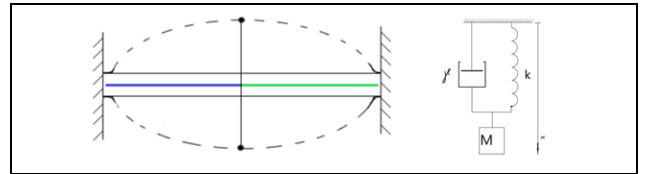
Figură 2.16 Schema sistemului echivalent cu masa concentrata pentru primul mod de vibrație

The system constructed for analyzing the first mode of vibration consists of a mass M, elastic constant k, and damping coefficient γ, as shown in Figure 2.16. The equation of motion, in the case of the arc deformation due to the displacement of the mass from the equilibrium position, is given by::

$$M\ddot{x} + \gamma\dot{x} + kx = 0 \qquad (2.60)$$

Taking into account that we want to derive the equation of motion in its general form, without considering the damping force, the equation becomes::

$$M\ddot{x} + kx = 0 \qquad (2.61)$$

which is a second-order homogeneous differential equation. The solution to such an equation is given by::

$$x = A_m \sin(\omega_n t + \varphi) \qquad (2.62)$$

$$f_n = \frac{1}{2\pi}\sqrt{\frac{k}{M}} \qquad (2.63)$$

$$A_m = \sqrt{x_0^2 + \left(\frac{v_0}{\omega_n}\right)^2} \qquad (2.64)$$

$$\varphi = arctg\frac{\omega_n x_0}{v_0} \qquad (2.65)$$
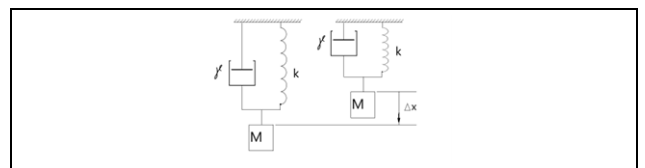
Figură 2.17 Sistemul modelat sub forma de masă concentrată scoasă din poziția de echilibru

$$T = \frac{1}{f_n} = \frac{2\pi}{\omega_n} \quad (2.66)$$

$$f_n = \frac{1}{2\pi}\sqrt{\frac{g}{\Delta x}} \quad (2.67)$$

According to [7], in the case of a bar fixed at both ends, the elastic constant is given by:

$$k = \frac{192EI}{(A+B)^3} \quad (2.68)$$

$$f = \frac{1}{2\pi}\sqrt{\frac{k}{M}} = \frac{1}{2\pi}\sqrt{\frac{\frac{192EI}{(A+B)^3}}{M}} \quad (2.69)$$

So, the length of the arms, the material, and their cross-section have the greatest impact. The mass has only a secondary role. As for the maximum deflection, it depends on:

$$A_{max} = \sqrt{x_0^2 + \left(\frac{v_0 M}{k}\right)^2} = \sqrt{x_0^2 + \left(\frac{v_0 M}{\frac{192EI}{(A+B)^3}}\right)^2} \quad (2.70)$$

And in the case of amplitude, the lengths of the arms, the material, and the shape of the bar have the greatest impact.

The system constructed for determining the second mode of vibration consists of two masses suspended by springs and dampers as shown in Figure 2.18..
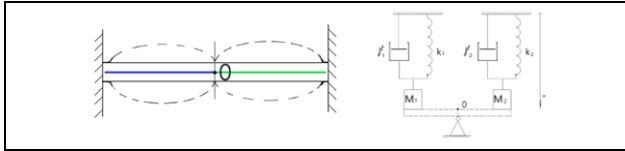
Figură 2.18 Mod 2 de vibrație (stânga) și sistem echivalent bazat pe tehnica maselor concentrate

$$M1\ddot{x}1 + \gamma 1\dot{x}1 + k1x1 = 0 \quad (2.71)$$
$$M2\ddot{x}2 + \gamma 2\dot{x}2 + k2x2 = 0 \quad (2.72)$$

Since the system needs to be in equilibrium at the stationary point M1=M2=M/2. The damping forces can be considered zero in this case, so $\gamma = 0$. Therefore, the equations of motion can be written as::

$$\frac{M}{2}\ddot{x}1 + k1x1 = 0 \quad (2.73)$$

$$\frac{M}{2}\ddot{x}2 + k2x2 = 0 \quad (2.74)$$

The equations are independent and allow for the solutions available for single-degree-of-freedom systems in the form of::

$$x_1 = A_{m1} sin(\omega_{N1} + \varphi_1) \quad (2.75)$$

and

$$x_2 = A_{m2} sin(\omega_{N2} + \varphi_2) \quad (2.76)$$

Knowing that the two masses move with the same frequency but in opposite directions and with the same amplitude, we can write:: $\omega_N = \omega_{N1} = \omega_{N2}, \varphi_1 = \frac{\pi}{2} + \varphi_2$ și $A_{m1} = A_{m2} = A_m$.

The equations become:

$$x_1 = A_m sin(\omega_N + \varphi) \quad (2.77)$$

and

$$x_2 = A_m sin\left(\omega_N + \varphi + \frac{\pi}{2}\right) \quad (2.78)$$

or, knowing $sin\left(\alpha + \frac{\pi}{2}\right) = \cos\alpha$, for any given angle $\propto$

$$x_2 = A cos(\omega_N + \varphi) \quad (2.79)$$

The angular frequency is: $\omega_n = \sqrt{\frac{2k}{M}}$.

Knowing that point O, Figure 2.18, is a nodal point and therefore fixed, we can consider it as clamped. Thus,:

$$k_1 = \frac{192EI}{A^3} \quad (2.80)$$

$$k_2 = \frac{192EI}{B^3} \quad (2.81)$$

$$x_1 = A_m sin\left(\sqrt{\frac{2\frac{192EI}{A^3}}{M}} + \varphi\right) \quad (2.82)$$

$$x_2 = A_m cos\left(\sqrt{\frac{2\frac{192EI}{B^3}}{M}} + \varphi\right) \quad (2.83)$$

$$f_1 = \frac{1}{2\pi}\sqrt{\frac{2k_1}{M}} = \frac{\sqrt{2}}{2\pi}\sqrt{\frac{\frac{192EI}{A^3}}{M}} \quad (2.84)$$

$$f_2 = \frac{1}{2\pi}\sqrt{\frac{2k_2}{M}} = \frac{\sqrt{2}}{2\pi}\sqrt{\frac{\frac{192EI}{B^3}}{M}} \quad (2.85)$$

and $f_1 = f_2$, because the oscillations only differ in phase, not in frequency. As for the maximum amplitude, considering x_{01}, x_{02} si v_0 as initial conditions with $x_{01} = -x_{02}$ elative to the static equilibrium point O, we find:

$$A_{m1-max} = \sqrt{x_{01}^2 + \left(\frac{v_0 M}{2k_1}\right)^2} = \sqrt{x_{01}^2 + \left(\frac{v_0 M}{\frac{384EI}{A^3}}\right)^2} \quad (2.86)$$

$$A_{m2-max} = \sqrt{x_{02}^2 + \left(\frac{v_0 M}{2k_2}\right)^2} = \sqrt{x_{02}^2 + \left(\frac{v_0 M}{\frac{384EI}{B^3}}\right)^2} \quad (2.87)$$

Deoarece $x_{01}^2 = x_{02}^2$ si $A = B$, rezultă bineînțeles ca $A_{m1-max} = A_{m2-max}$, iar

$$\varphi = arctg\frac{\omega_n x_{01}}{v_0} = arctg\frac{\omega_n x_{02}}{v_0} \quad (2.88)$$
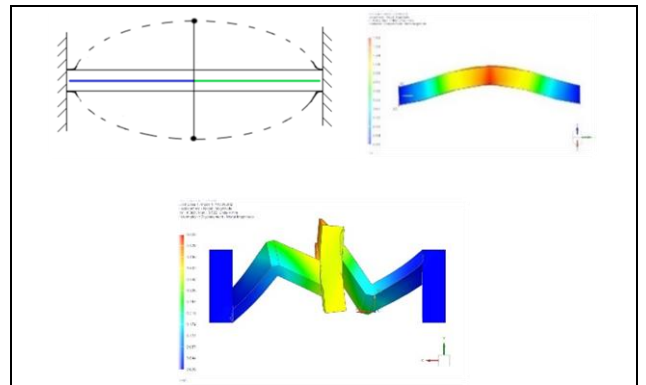
Figură 2.19 Analiza modală: modul 1 de vibrație. Stânga sus modelul analitic, dreapta sus modelul de legătura, jos simularea modelului real

The idealized system developed for the analytical study of vibration modes is validated with the CAD/CAE model. Both models start with the idea of discretizing the system by dividing it into a finite number of elements. The calculated modes correspond to the natural frequencies of the body. Figure 2.19 brings together the three models in the case of the first mode of vibration.
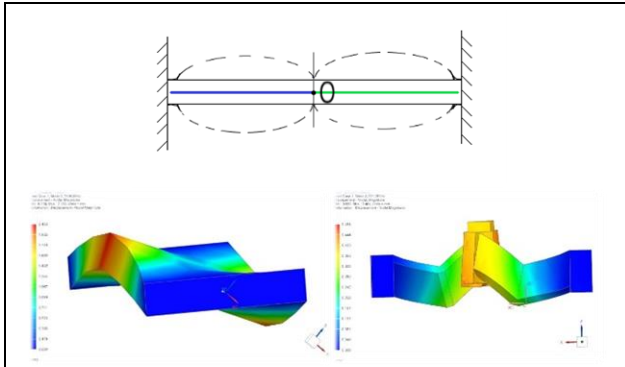
Figură 2.20 Analiza modală: modul 2 de vibrație. Stânga sus modelul analitic, dreapta sus modelul de legătura, jos simularea modelului real

In the case of the second mode of vibration, the numerical analyses are in agreement with the analytical representation. The differences are small and are represented in the simulation of the real model by a torsional component present between the connections of the arms on the movable carriage. This torsional mode can be reduced or even eliminated by redesigning the carriage and the connection mode of the arms.

Figure 2.20 presents the second mode of vibration. A direct agreement can be identified between the analytical representation and the FEM simulation of the connection model..

2.8 Flexible strips

The bearings of the arms are made up of pivots constructed with flexible elements, which according to [4], provide high endurance, lack of play, immunity to wood chips and sawdust, and exceptional cost-effectiveness. Each element has a length (l) of 51mm, a width (u) of 20mm, and a thickness (t) of 0.4mm. If we consider the base width as (w) and the distance

between two bars as (r), according to [8], the system can be determined by:

$$l = w\sqrt{1 + \left(\frac{r}{w}\right)^2} \qquad (2.89)$$

The bending resistance of the pivot can be modeled as a torsion spring.:

$$K = \frac{kEI}{2l} \qquad (2.90)$$

Where E is the Young's modulus, l is the length of the flexible element, I is the moment of inertia of the cross-sectional area of the flexible element, and k is the stiffness coefficient, which according to [8], is given by:

$$k = 5.300185 - 1.6866\frac{r}{w} + 0.88536\left(\frac{r}{w}\right)^2 - 0.2094\left(\frac{r}{w}\right)^3 + 0.018385\left(\frac{r}{w}\right)^4 \quad (2.91)$$

The lifespan of the pivot is directly proportional to the stress in the flexible strip [9], and according to [8], the maximum value is expressed as::

$$\sigma = \frac{S\theta EI}{2r} \qquad (2.92)$$

where θ is the maximum angle of deflection of the strip during pivoting, and S is the stress coefficient defined as::

$$S = 0.062998 + 1.884218\frac{r}{w} - 1.43653\left(\frac{r}{w}\right)^2 + 0.551786\left(\frac{r}{w}\right)^3 - 0.10523\left(\frac{r}{w}\right)^4 +$$
$$0.007889\left(\frac{r}{w}\right)^5 \qquad (2.93)$$

By using the finite element method, the Nastran solver, and the SOL 101 solution, we can identify how the strips behave based on w and l when r is kept constant..
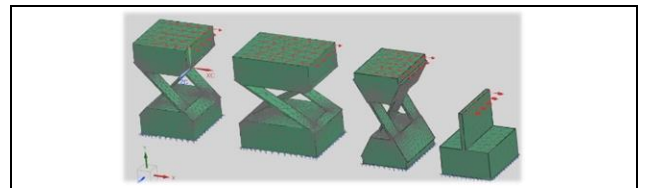
Figura 2.21 Meșa pivoților cu diferiți w și l

Figure 2.21 shows the discretization and applied loads to the model. It consists of several test specimens with different base widths of the strips and different lengths of the strips.
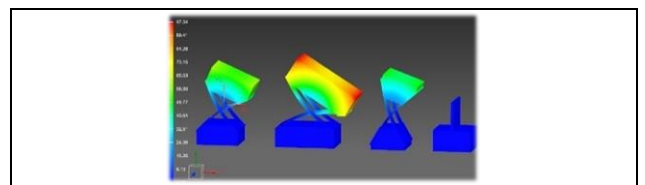
Figura 2.22 Analiza FEM a celor 4 specimene – săgeata maxima

Figure 2.22 indicates the maximum displacement of the test specimens. It can be

easily observed that as the angle between the strips increases, the reached angle also increases..
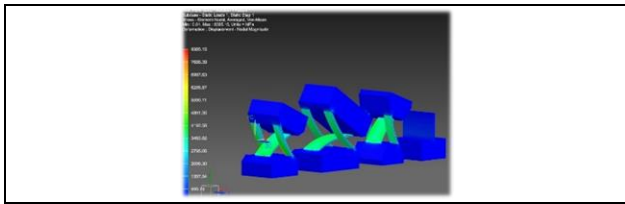
Figura 2.23 Analiza FEM a celor 4 specimene – stresul sub încărcare orizontala

Figure 2.23 indicates that the stress in the strips is almost the same in all cases. In this scenario, the lifespan of the strips can be considered equal when subjected to the same horizontal force during bending. Since the specimen with 120 degrees between the strips has the largest angle, it seems to be the best choice..
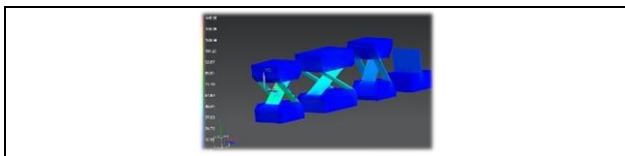
Figura 2.24 Analiza FEM a celor patru specimene sub încărcare verticala

Indeed, as shown in Figure 2.24, the stress under vertical loading is no longer identical. The larger the angle between the strips, the higher the stress caused by the load. This indicates that the choice of angle between the strips can have a significant impact on the stress distribution and, consequently, on the durability of the strips under vertical loading conditions. Therefore, it is important to carefully consider the design parameters, such as the angle between the strips, in order to ensure optimal performance and longevity of the system..
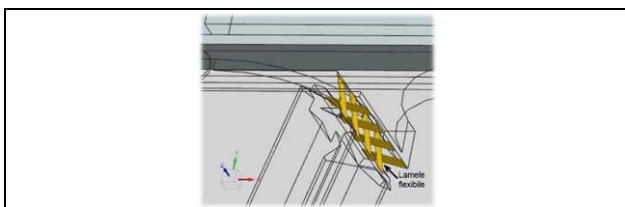
Figura 2.25 Articulație pivotantă cu patru perechi de lamele

As shown in Figure 2.25, a favorable result can be achieved with a minimum of four pairs of strips per pivot. This configuration allows for improved stability and load distribution. Regarding the assembly of the strips, securing them using screws can provide nanometric precision if certain important rules are

followed. The pressure cones of the screws should overlap, and the outer parts should avoid generating stress concentration by rounding the edges near the strips, as illustrated in Figure 2.26. These guidelines help to ensure proper alignment, minimize stress concentrations, and enhance the overall performance and durability of the assembly..
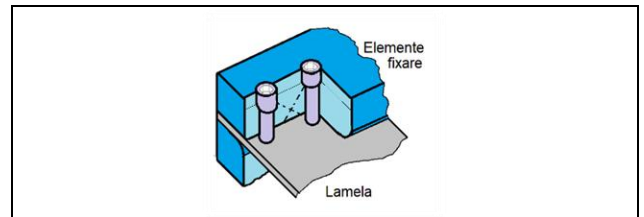
Figura 2.26 Prindere lamela flexibila prin intermediul șuruburilor

Another method of blade fixation is generated by the possibility of using welding as a fastening element. Only electric arc welding can provide satisfactory results. Cutting the steel blades is done using electroerosion machines or water jet machines. As mentioned earlier, blade installation is a process that can lead to errors and requires special clamping elements. To eliminate these inconveniences, this work introduces two new solutions for achieving compliant elements, namely: flexible blades obtained through mechanical processing of threaded bars and direct use of threaded bars as compliance-generating elements (Figure 2.27)..
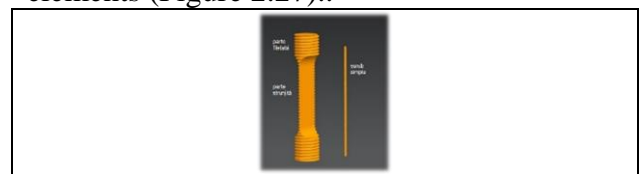
Figura 2.27 Lamelă Flexibilă obținută prin strunjirea unui șurub M30-stânga; șurub simplu M3-dreapta

In the first case, the strip fixation is greatly simplified because the thread is integrated with it. Fixation can be done directly using threaded assembly components, eliminating the possibility of strip rotation, mechanical stress caused by tightening, or mismatching of the pressure cones of the fastening screws.
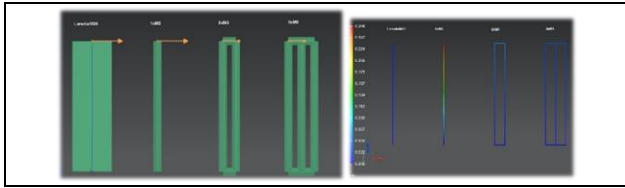
Figura 2.28 Meșa si analiza FEM în cazul încărcării laterale pentru specimenele: șurub M30 strunjit, șurub M3 simplu, dublu șurub M3 si triplu șurub M3
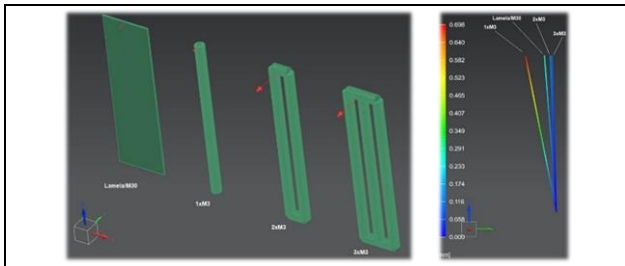
Figura 2.29 Meșa și analiza FEM în cazul încărcării frontale pentru specimenele: șurub M30 strunjit, șurub M3 simplu, dublu șurub M3 si triplu șurub M3

2.9 Optimisation

The shape and manufacturing materials of the arms are of significant importance. In order to increase bending and torsional rigidity, the structure shown in the figure below has been developed.:
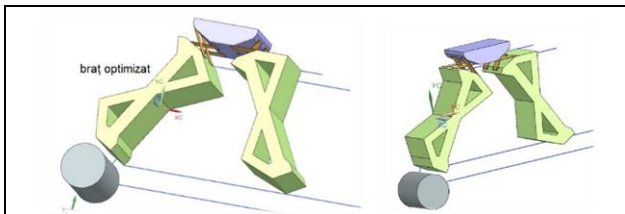
Figura 2.30 Sistem de brațe optimizate pentru creșterea rigidității la încovoiere si torsiune

2.10 Materials

The arms can be made of three types of materials, depending on the application: polymers (Figure 2.32), metal profiles, or composite materials. The most satisfactory result obtained after successive trials was represented by the combination of 1/3 volume of epoxy resin, composed of 1/2 hardener and 1/2 resin, and 2/3 volume of granular material. The tests resulted in the specimen shown in Figure 2.31.

Figura 2.31 Specimen de test din granit epoxidic
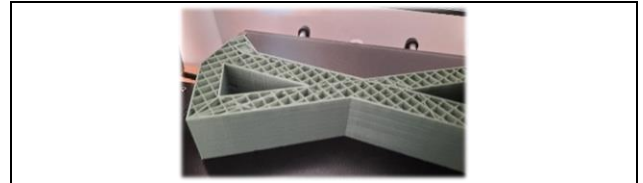
Figura 2.32 Specimen de test din material polimeric

2.11 System Layout

The analyzed arm system can be integrated into a solution with 2 or 4 arms. Figure 2.33 illustrates a system with 4 arms.
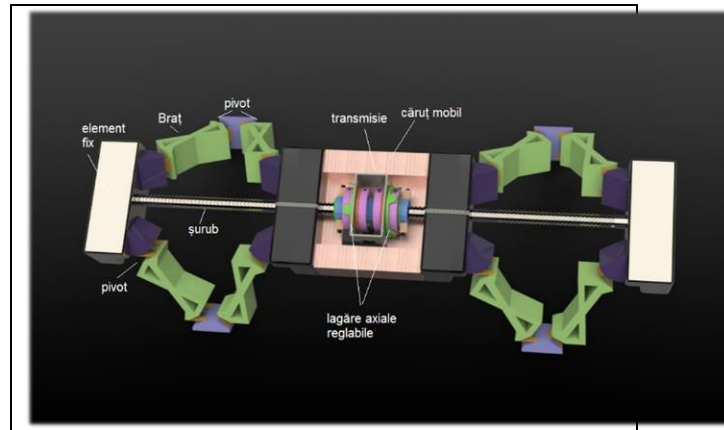
Figură 2.33 Sistem liniar cu patru brațe

2.12 Conclusions

Regarding the linear guidance system, considering the premise of a cost-effective solution focused on low cost, accuracy, reduced mass, and low maintenance, research has led to the development of an innovative system composed of multiple arms connected by angular joints. The achieved performances are as follows:

Low cost: approximately 35E for the polymer variant, approximately 45E for the metal profile variant, and approximately 120E for the epoxy granite variant.

Accuracy: precision and repeatability are directly related to the bending stiffness differences of the blades forming the joints. By simply adjusting the width of the stiffer blades through polishing after assembly, the desired

precision performance can be achieved. Angular deviations can be easily checked using a laser pointer against a wall at a distance of a few meters.

The mass of the guide varies depending on the construction as follows: polymer construction: 1.4kg, metal profile construction: 2.1kg, epoxy granite construction: 9.7kg. For reference, a conventional guide of similar characteristics made of cast iron weighs approximately 17kg. The system does not contain maintenance-requiring elements. For reference, a conventional system may require monthly bearing maintenance.

The lifespan is approximately 150,000 operating hours if steel spring blades are used. The lifespan depends on the ability of the blades to withstand repeated bending.

Capitolul 3 –DC brushless motor controller design and development

3.1 Introducere

This chapter aims to develop a servo system for actuating a linear axis that will be used in the construction of a production machine based on Industry 4.0 concepts.

The main part of this work is dedicated to the design of the PCB board belonging to the servo motor system. The design follows the most cost-effective path while maintaining the necessary quality to achieve good motor control. The circuits have been designed following the manufacturer's instructions, the ODrive 3.5 scheme, and the specific requirements of the axis. The electronic board design was done from scratch..

3.2 Fabrication rules

The elements of the electronic board must comply with the manufacturing capabilities of the factory that will produce it. As the project aims for cost optimization, the constraints should be met by the majority of manufacturers within regular production processes. There are

several production constraints that need to be fulfilled. The most important ones are described below.:

- Clearances
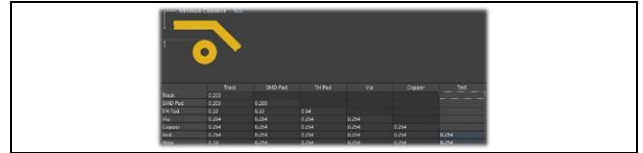
Figura 3.1 – Degajări

- Trace width

Figura 3.2 - Lățimi

- Via

Figura 3.3 - Via dimensiuni

- Differential pair

Figura 3.4 – Dimensiuni perechi diferențiale

- Vertical Alignment

Figura 3.5 – Degajări poziționare componente

3.3 Caracterizare termică

Thermal effects have a remarkable impact on the performance of electronic components. Each IC component on the board is a good candidate for thermal analysis, along with some passive components that are part of the power stage.:

Figura 3.6 - SMD component caracterizare termică

The thermal characteristic of components is primarily described by the thermal resistances found within them and within the junction layers. Firstly, there are θJC - the thermal resistance between the substrate and the package (enclosure), θCA - the thermal resistance between the package and the air surrounding it, θJB - the thermal resistance between the substrate and the PCB on which the IC is mounted, θJA - the thermal resistance between the substrate and the air surrounding the substrate package. The temperatures of interest are TJ - junction temperature, TC - package temperature, TA - ambient temperature (air around the package), TB - board temperature near the component.

According to its datasheet [1], the STM32F405 has a maximum power dissipation (PD) of 435mW and a maximum junction temperature (TJ) of only 105°C. To understand the required PCB surface area to keep the device at a safe temperature below 80°C, Ansys IcePak will be used to simulate a double-sided FR4 PCB with a 1 oz. copper layer and 50% copper on both sides to compensate for the traces beneath and around the chip..

Figura 3.7 - PCB caracterizare termică

Figura 3.8 - STM32F405 Distributia termica pe un PCB cu 2 straturi - Top view (stânga) and Bottom view (dreapta)

Figura 3.9 - STM32F405 vectorii viteza – convecție naturală

The simulation indicates a chip temperature of approximately 40°C and a surface area of about 4 square centimeters on the top and bottom of the PCB.

The DRV8301 is a complex circuit. To obtain an estimate, the focus will be on calculating the power loss in the major components of the chip in a theoretical regime: inputs, output buffer, buck regulator, LDOs, internal logic. The data for the calculations will be provided by the device datasheet [2]. Since only a reasonable estimate is required at this stage, and since power loss is directly proportional to the regulator's efficiency, a simple solution could be found by estimating the regulator's efficiency and relating it to the output power generated using the efficiency formula.:

$$\eta = \frac{P_{OUT}}{P_D + P_{OUT}} \tag{3.1}$$

P_D is:

$$P_D = P_{OUT}\left(\frac{1-\eta}{\eta}\right) \tag{3.2}$$

The efficiency of buck regulators, such as the one found in the DRV8301, is typically between 90% and 95%. To have a safe margin of error, we will use an efficiency of 90%. The regulator will provide a maximum of 1A at 5V, so POUT is around 5W. PD is then given by:

$$P_D = 5W * \left(\frac{1-0.90}{0.90}\right) = 0.56W \tag{#3.3}$$

The DRV8301 has two LDOs, AVDD and DVDD, whose power dissipation can be calculated by considering the output current and voltage drop.:

$$P_D = I * (V_{IN} - V_{OUT}) \tag{3.4}$$

For AVDD, the output voltage is 6.5V, and the supplied current is estimated to be 2mA.

$$A_{VDD} = (24V - 6.5V) * 0.002A = 0.035W \tag{3.5}$$

16

For DVDD, the output voltage is 3.3V, and the supplied current is estimated to be 5mA..

$$D_{VDD} = (24V - 3.3V) * 0.005A = 0.15W \qquad (3.6)$$

For the internal logic of the DRV, we can estimate a power consumption of only 0.1W..

The calculation of total power loss.:

$$0.06W + 0.01W + 0.56W + 0.035W + 0.1W = 0.765W \qquad (3.7)$$

Figura 3.10 - DRV8301 Distribuție termică fără via termice – Top view (stânga) and Bottom view (dreapta)
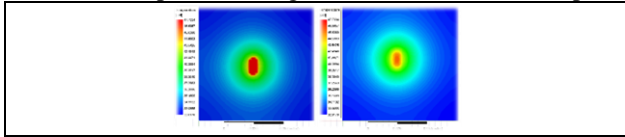
Figura 3.11 - DRV8301 Distribuție termica cu via termice - Top view (stânga) and Bottom view (dreapta)

The impact of thermal paths becomes immediately evident when comparing Figure 3.10 and Figure 3.11. AZ1117EH is a simple LDO regulator whose power dissipation can be easily obtained by considering the voltage drop and maximum output current..

$$P_D = I * (V_{IN} - V_{OUT}) \qquad (3.8)$$
$$P_D = 0.270A * (5V - 3.3V) = 0.459W \qquad (3.9)$$
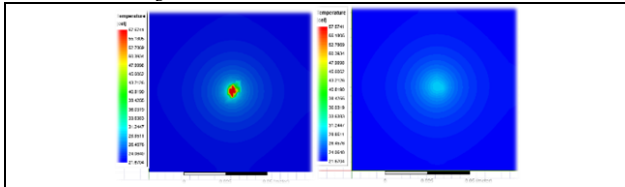
Figura 3.12 - AZ1117EZ Distribuție termica - Top view (stânga) and Bottom view (dreapta)

The simulation indicates a maximum on-board temperature of approximately 58°C (Fig. 3.12).

Bulk capacitors:
The lifespan of an electrolytic capacitor is directly related to its internal temperature. Each 10-degree Celsius increase in internal temperature reduces the component's lifespan by half.

According to [5], the dielectric losses (Pdielectric) are as follows::

$$P_{dielectric} = \hat{u}_{ac}^2 * \pi * f_0 * C * \tan \delta_0 \qquad (3.10)$$

ûac - peak value of the symmetric AC voltage applied to the capacitor [V]
f0 - fundamental frequency in Hz of the ripple voltage
C - capacitance
tan δ0 - dielectric dissipation factor

$$P_{dielectric} = 2^2 V * \pi * 120Hz * 470 * 10^{-6}F * 0.12 = 0.085W \qquad (3.13)$$

Resistive losses are according to [6]:

$$P_{resistive} = I_{rms}^2 * ESR \qquad (3.14)$$

I rms - Root Mean Square (RMS) value of the capacitor current
ESR - Equivalent Series Resistance in ohms

The Equivalent Series Resistance (ESR) is the sum of the ohmic losses of the dielectric, materials, and connections used in the construction of the capacitor. It can be easily determined based on tan δ_0..

$$ESR = \tan \delta_0 * X_C = \frac{\tan \delta_0}{2 * \pi * f_0 * C} \qquad (3.15)$$

$$ESR = \frac{0.12}{2 * 3.1415 * 120Hz * 470 * 10^{-6}F} = 0.338 ohm \qquad (3.16)$$

The RMS value of the ripple current is not as straightforward to determine. It depends on the inductance (L) and resistance (R) of the motor windings, the time constant of the winding (τ = L/R), the motor's operating condition, the applied voltage (VDCBUS), the PWM period (T), electromotive force (EMF), and the duty cycle (D)..
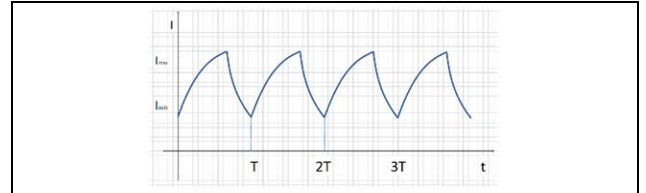
Figura 3.13- Curent ondulatoriu PWM

$$P_{resistive} = I^2 * ESR \qquad (3.17)$$

$$I_{ON}(t) = I_{min}e^{\frac{-t}{\tau}} + \frac{V_{DCBUS} - E}{R}\left(1 - e^{\frac{-t}{\tau}}\right) \qquad (3.18)$$

$$I_{OFF}(t) = I_{max}e^{\frac{-(t-DT)}{\tau}} - \frac{E}{R}\left(1 - e^{\frac{-(t-DT)}{\tau}}\right) \qquad (3.19)$$

Selecting Imin and Imax on the ION and IOFF curves, respectively, we obtain:

$$I_{ON}(DT) = I_{max} \quad and \quad I_{OFF}(T) = I_{min} \qquad (3.20)$$

Solving for these points:

$$I_{min} = -\frac{E}{R} + \frac{V_{DCBUS}}{R} * \left(\frac{e^{\frac{(1-D)T}{\tau}} - e^{\frac{T}{\tau}}}{1 - e^{-\frac{T}{\tau}}}\right) \qquad (3.21)$$

$$I_{max} = -\frac{E}{R} + \frac{V_{DCBUS}}{R} * \left(\frac{1 - e^{-\frac{DT}{\tau}}}{1 - e^{-\frac{T}{\tau}}}\right) \qquad (3.22)$$

we get the ripple current

$$I_{max} - I_{min} = \frac{V_{DCBUS}}{R} * \frac{\left(1 - e^{-\frac{T}{2\tau}}\right)^2}{1 - e^{-\frac{T}{\tau}}} \qquad (3.23)$$

$$V_{DCBUS} = 20V; \quad R = 150 * 10^{-3} Ohm;$$
$$\tau = 0.167 * 10^{-3} s; \quad T = 4.2 * 10^{-5} Hz \qquad (3.24)$$

$$I_{max} - I_{min} = \frac{V_{DCBUS}}{R} * \frac{\left(1 - e^{-\frac{T}{2\tau}}\right)^2}{1 - e^{-\frac{T}{\tau}}} \cong 8.5\ A \qquad (3.25)$$

$$I_{rms} = \frac{I_{ripple}}{\sqrt{3}} \cong 4.8A \qquad (3.26)$$
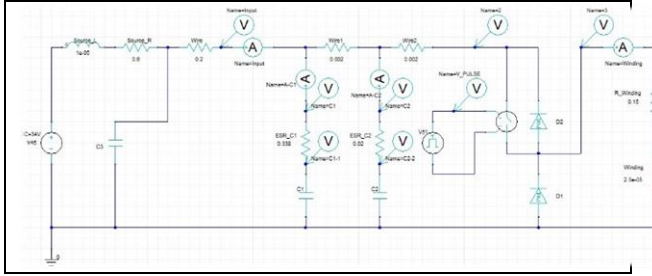
Figura 3.14 – Simulare condensatoare în Ansys Nexxim

The current through the bulk capacitors, along with the total current through the winding, is graphically represented in Figure 3.15..
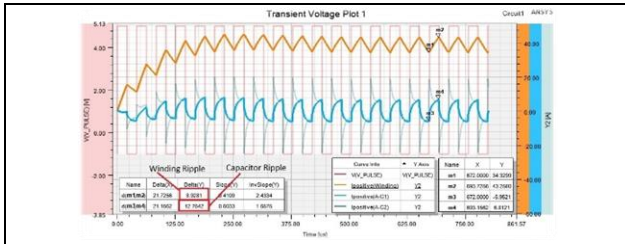
Figura 3.15 – Curenții circuitului: Curentul înfășurării în oranj, curentul în capacitorul de 470uF în albastru, curentul pe capacitorul de 10uF în albastru închis și tensiunea tăiată în roșu
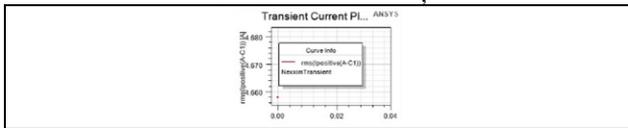
Figura 3.16- capacitor 470uF valoare rms
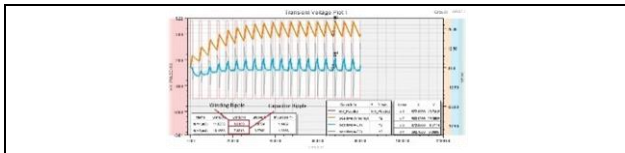
Figura 3.17- Simulare cu "duty cycle" 23% și un curent maxim în înfășurare de 30A

Figure 3.18 shows the new calculated RMS value after resuming the simulation. It indicates a value of 2.6A, which is 40% lower than the previous value..
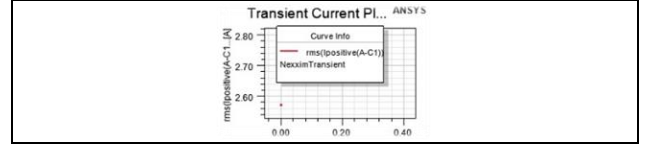
Figura 3.18   Valoare Rms a capacitorului 470uF pentru al doilea caz

$$P_{resistive} = I_{rms}^2 * ESR = 1^2 A * 0.338 ohm \cong 0.4W \qquad (3.27)$$

In addition to resistive power loss, there is also dielectric loss.:

$$P_{tot} = 0.085W + 0.4W = 0.485W \qquad (3.28)$$
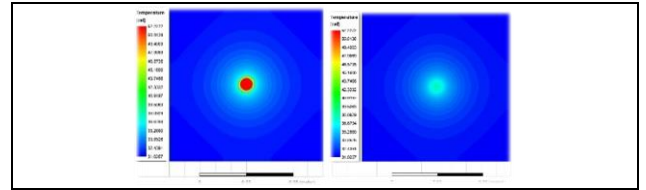
Figura 3.19 Capacitoarele Bulk - Distribuția tensiunii - Top view (stânga) and Bottom view (dreapta)
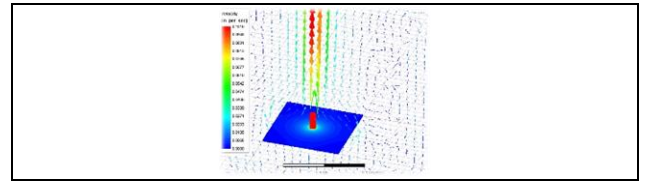
Figura 3.20 Capacitoarele Bulk -convecție naturală – vectorii vitezei

The current sensing resistors have a value of 2mOhm and will experience a peak current of up to 30A flowing through them. Taking into account that the current waveform is a sinusoid composed of a fundamental frequency of 24 kHz and the third harmonic at 72 kHz, we can estimate an RMS value of 22A. The power dissipated as heat will then be 0.96W. These devices are located in close proximity to the power transistors and will be simulated together with them.

$$P_D = P_{RDS} + P_{switch} + P_{diode} \qquad (3.29)$$

The power dissipated during the ON states is relatively easy to estimate.:

$$P_{RDS} = R_{DS(ON)} * I_{rms}^2 \qquad (3.30)$$
$$R_{DS(ON)} = 1.7 mohm * 1.65 = 2.8 mohm \qquad (3.31)$$
$$P_{RDS} = (22A)^2 * 2.8 mohm = 1.36W$$

According to [9], the switching losses are:

$$P_{switch} = P_{rise} + P_{fall} \qquad (3.33)$$
$$P_{rise} = \frac{V_M * I_{rms} * f_{switch} * t_{rise}}{2} \qquad (3.34)$$
$$P_{fall} = \frac{V_M * I_{rms} * f_{switch} * t_{fall}}{2} \qquad (3.35)$$

We can calculate the rise and fall based on the equations found in [10].:

$$t_{rise} = \frac{Q_{GD}}{I_{source}} = \frac{4.7nC}{0.7A} = 6.7ns \qquad (3.36)$$

$$t_{fall} = \frac{Q_{GD}}{I_{sink}} = \frac{4.7nC}{0.7A} = 6.7ns \qquad (3.37)$$

$$P_{rise} = \frac{20V * 22A * 24000Hz * 6.7 * 10^{-9}s}{2} = 0.035W \qquad (3.38)$$

$$P_{fall} = \frac{20V * 22A * 24000Hz * 6.7 * 10^{-9}s}{2} = 0.035W \qquad (3.39)$$

The power loss within the diode is:

$$P_{diode} = R_{diode} * I_{rms}^2 * duty \qquad (3.40)$$

$$P_{diode} = 7.5mohm * (22A)^2 * 0.01 = 0.036W \#(3.41)$$

The total power dissipated inside the transistor chip is:

$$P_D = P_{RDS} + P_{switch} + P_{diode} = 1.36W + 0.035W + 0.035W + 0.036W \cong 1.5W \qquad (3.42)$$

Figure 3.21 shows the heat distribution in the case of a MOSFET and its corresponding feedback resistor.
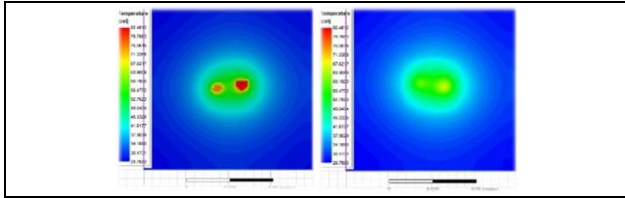
Figura 3.21 MOSFET(dreapta în fiecare figura) și rezistențele de feedback (stânga în fiecare figură) – Distribuție termică cu 1 via termic per 4mm² - Top view (stânga) and Bottom view (dreapta)
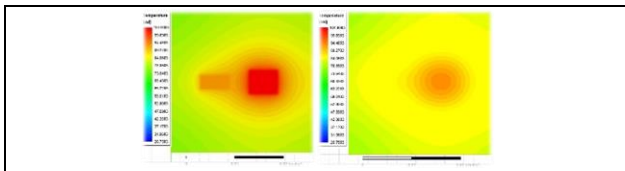
Figura MOSFET(dreapta în fiecare figură) și rezistențele de feedback (stânga în fiecare figură) – Distribuție termică PCB 30x30mm cu 1 via termic per 4mm2- Top view (stânga) and Bottom view (dreapta)

Each device requires a certain amount of space on the PCB to ensure proper cooling. Several arrangements have been attempted based on trial and error.
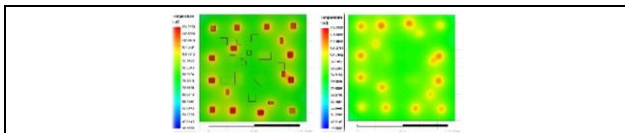
Figura 3.22- Toate componentele pe PCB cu 1 via termic per 4mm2- Top view (stânga) and Bottom view (dreapta)

In these circumstances, the solution to the mentioned problem could involve increasing the size of the board, using forced air flow over the board, mounting heat sinks over the

transistors, or a combination of the above. Figure 3.23 and Figure 3.24 show the simulation results when an air flow of 0.25 m/s is blown over the board.
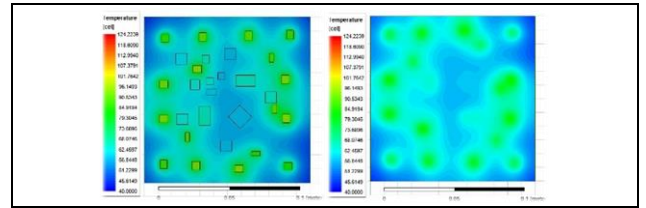
Figura 3.23 Toate componentele poziționate pe PCB cu1 1 via termic per 4mm2 și convecție forțată de 0.25m/s perpendicular pe fața plăcii- Top view (stânga) and Bottom view (dreapta)
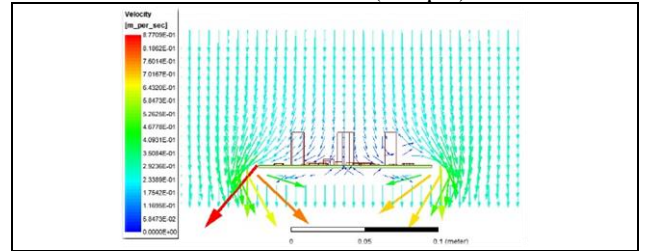
Figura 3.24 – Vectorii convecției forțate

Mounting heat sinks on the transistors brings the board into a safe operating temperature zone. The initial simulations are conducted with a single transistor with an attached heat sink and a current sensing resistor on a 3cmx3cm PCB with 90% coverage of 1 oz. copper plating on each side and a thermal via every 4 mm2. The heat sink has a base size of 14mmx14mm, a height of 6mm, and features 7 fins. The ambient temperature is set at 20 degrees Celsius..
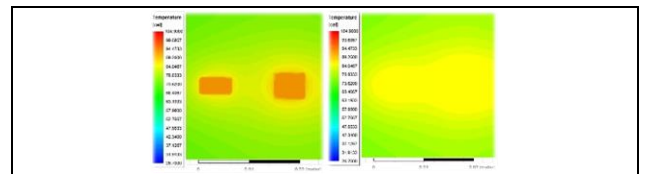
Figura 3.25 MOSFET(dreapta în fiecare figură) și rezistentele de feedback (stânga în fiecare figură) – Distribuție termică PCB 30x30mm cu 1 via termică per 4mm2 cu radiator poziționat pe transistor- Top view (stânga) și Bottom view (dreapta)
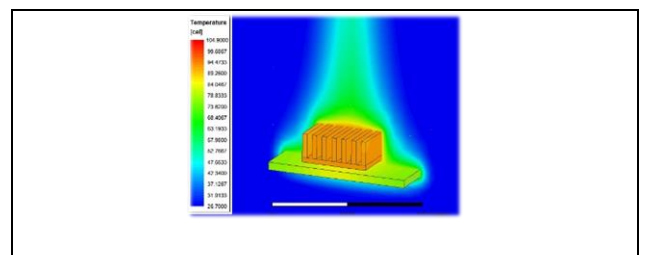
Figura 3.26 Distribuția termică pe radiatorul transistorului

The final placement of the components will be based on the analysis of the heat distribution conducted so far and must also incorporate solutions for the electrical constraints of the design.
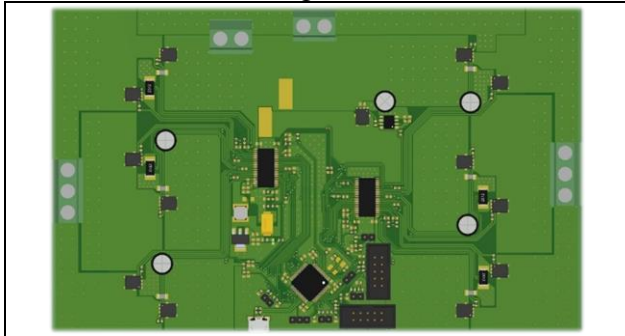
Figura 3.27 PCB - Schiță Layout

Figure 3.28 shows the simulation results for the top and bottom sides of the layout sketch. We obtain the same results as in the previous simulation (see Figure 3.28). As expected, to achieve our maximum temperature goal of 100 °C, external means of heat dissipation are required: external forced air, heat sinks, or both..
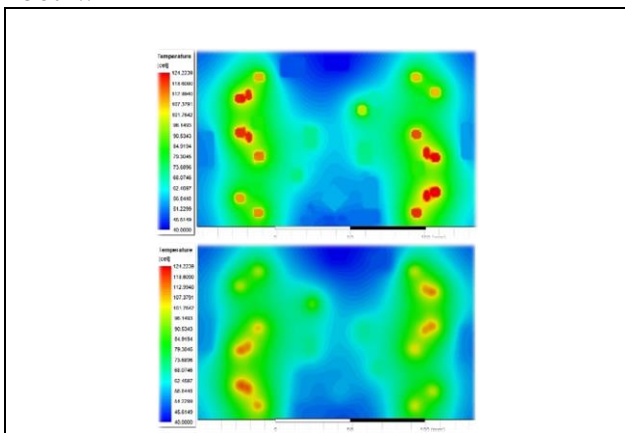
Figura 3.28 PCB Harta termică pe un PCB dublu strat cu 1 via termica per 4mm2 - Top view (stânga) și Bottom view (dreapta)

3.4 Power Integrity Analysis

The power supply for the board essentially needs to provide adequate electrical power to all the logic devices and a stable voltage reference for the exchange of information in the form of both digital and analog signals..

3.4.1 DCIR Analysis

A first basic analysis relates to the amount of energy lost in the copper traces.
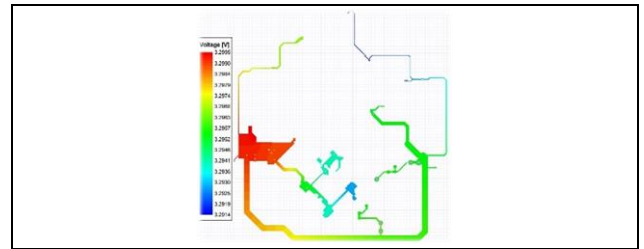
Figura 3.29 Analiza DCIR a tensiunii de 3.3VDC

The maximum voltage difference on the board is 8.1 mV, with minimum and maximum values of 3.2914V and 3.2999V, respectively. These values allow all systems to operate correctly (Fig 3.29)..

3.4.2 Power Impedance and noise

The rising and falling edges of the waveform generate current fluctuations and, consequently, voltage fluctuations across the inductances encountered along its path, expressed as:

$$V\ fluctuation = L \times di/t\ raise/fall \qquad (3.43)$$

As a general rule, the spectrum can be quickly calculated using the formula below [10]:

$$f_{knee} = 0.5/\ t\ raise/fall \qquad (3,44)$$
$$f_{knee} = 100MHz,\ for\ t\ raise/fall\ of\ 5ns \qquad (3.45)$$

Yes, this formula can be used to understand where the highest energy of the digital pulses is concentrated. By calculating the spectrum, you can analyze the frequency components and identify the frequency ranges where the majority of the energy of the digital impulses is concentrated. This information can be valuable for designing appropriate filtering and decoupling techniques to mitigate any unwanted effects caused by these high-frequency components..

$$V_{noise} = Z_{PDN}(f) * I_{noise} \qquad (3.46)$$

Where ZPDN is the PDN impedance and Inoise is the maximum transient load..

$$Z_{PDN} = 100mV/150mA = 0.67ohm,\ pentru\ partea\ digitala\ și$$
$$Z_{PDN} = 16.5mV/150mA = 0.11ohm,\ pentru\ partea\ analogică$$

In order to achieve the target impedance, we need to calculate the system impedance across the entire spectrum..
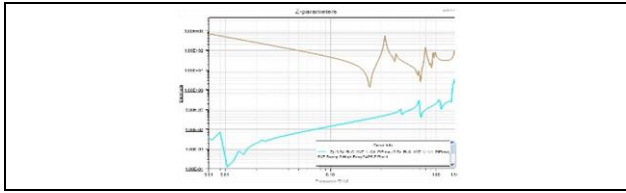
Figura 3.30 Impedanța PDN la MCU fără VRM: bare board (maro); cu capacitoare (albastru)

$$ZVRM \approx 2\pi fLVRM < 0.01 \, ohm \qquad (3.47)$$

From the kilohertz range to tens of kilohertz, the VRM inductance and the inductance of cables/traces start to become significant. An estimate of the required value at this level is provided by the following formula [11].:

$$C_{bulk} \geq \frac{1}{2\pi f \sqrt{Z_T^2 - ESR^2}} \qquad (3.48)$$

Where f is the minimum frequency of the interval, ZT is the target impedance we aim for, and ESR is the total resistance of the capacitor, typically having values lower than 50 mΩ..

$$C_{bulk} \geq \frac{1}{2\pi * 50000 \sqrt{0.67^2 - 0.005^2}} \sim 4.7 * 10^{-6} F \qquad (3.49)$$

$$f_{high} = \frac{\sqrt{Z_T^2 - ESR^2}}{2\pi ESL} \qquad (3.50)$$

Where ESL is the capacitor's inductance. Typically, ESL for such a capacitor would have a value of approximately half a nanohenry (nH).

$$f_{high} = \frac{\sqrt{0.67^2 - 0.005^2}}{2\pi * 4 * 10^{-10}} \sim 270 * 10^6 Hz \qquad (3.51)$$
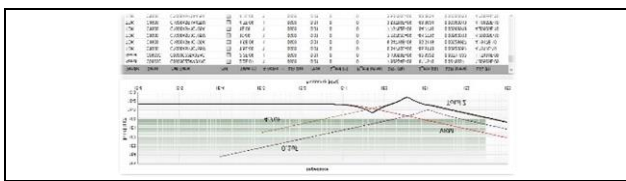
Figura 3.31 Impedanța VRM, capacitoare și Z total – fără placa

Figure 3.31 shows a possible solution for an energy storage area.
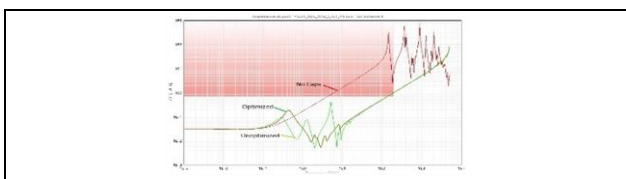
Figura 3.32 PDN la alimentarea MCU cu VRM și placa- fără capacitoare (rosu), neoptimizat (verde), optimizat (maro)

Figure 3.32 shows our initial solution, while Figure 3.33 presents the optimized solution.

Figura 3.33 PDN soluție optimizată a capacitoarelor

3.4.3 Resonance

Figure 3.34 presents the relevant resonance modes and frequencies..
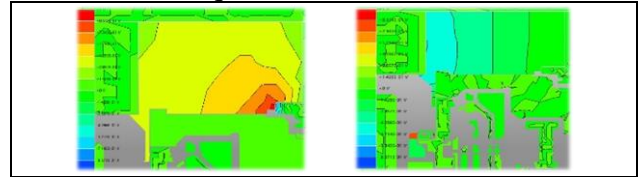
Figura 3.34 Moduri rezonante pentru tensiune și retur pe o porțiune mică a plăcii unde acestea apar ca planuri de alimentare - 126kHz stânga și 296MHz dreapta

3.5 Signal Integrity Analysis

Signal Integrity (SI) analysis deals with the quality of information transmitted and received in the form of analog electrical quantities..
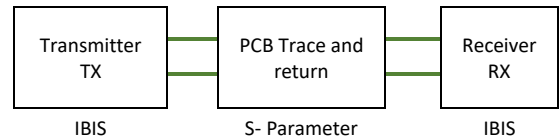
Figura 3.35 Simulare în domeniul timp utilizând IBIS și parametrii – S
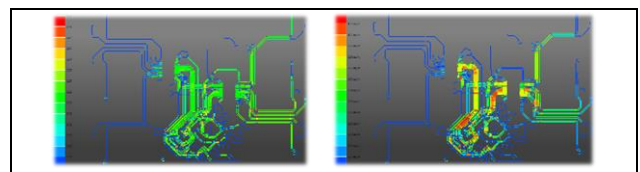
Figura 3.36 Interferența la nivelul plăcii - NEXT (Near End Crosstalk)-stânga; FEXT (Far End Crosstalk) – dreapta

The significant crosstalk locations are highlighted in red.

Analog signals analysis
The current motor feedback signals are crucial analog signals for the proper operation of the electronic device, so correct routing is mandatory. The analog feedback sent from the

two DRV8301s to the MCU is first analyzed (Fig 3.37).
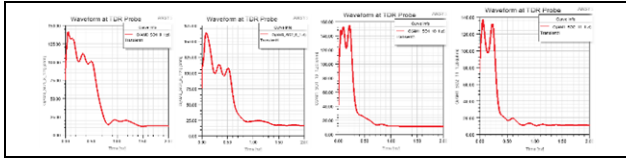
Figura 3.37 Analiza TDR a feedback-urilor curenților procesați; de la stânga la dreapta – M0_SO1, M0_SO2, M1_SO1, M1_SO2

The oscillator lines. Figure 3.38 presents the schematic and layout..
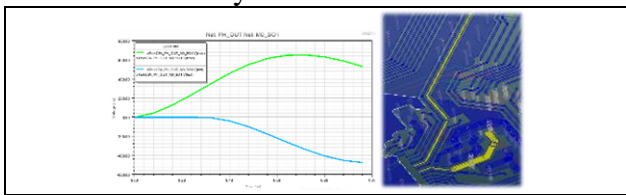
Figura 3.38 *Crosstalk*: Liniile oscilatorului vs feedback curent (M0_SO1)-stânga; layout – dreapta

Analiza arată un impact moderat asupra liniei analogice. În continuare, vom verifica impactul semnalului PWM asupra liniilor analogice. Rezultatul este prezentat în Figura 3.39.
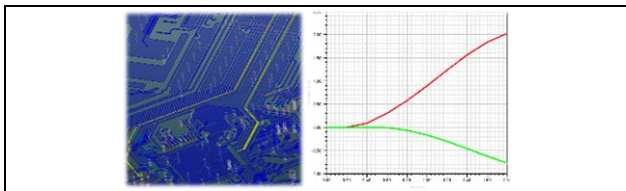
Figura 3.39 Interferența între traseele PWM și traseele analogice M0

The crosstalk analysis indicates an induced voltage of approximately 2 millivolts..

3.5.1 PWM signal analysis

The PWM signals carry the switching information to the motor driver..

Figura 3.40 M0_AH – Caracterizarea traseelor în formă tabelară
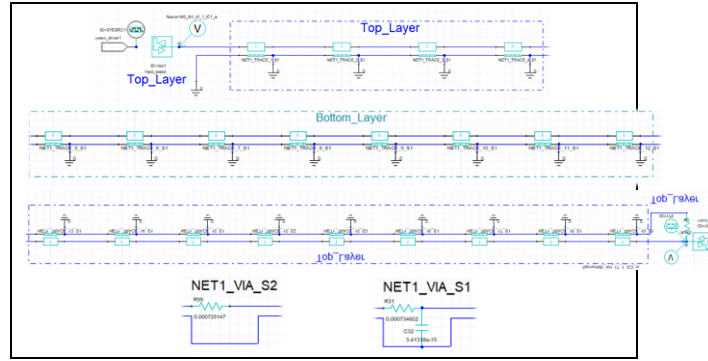
Figura 3.41 Traseu PWM (M0_AH) - caracterizare

Figure 3.41 presents the characterization of the M0_AH signal transmission line. Both Figure 3.42 and Figure 3.43 provide vital insights for the designer regarding the electrical characteristics of the signal path..
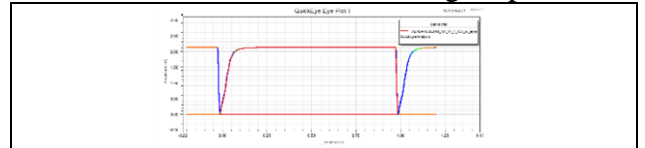
Figura 3.42 M0_AH – analiza Quick Eye

Figura 3.42 ajută la identificarea posibilei degradări a semnalului la capătul receptorilor.
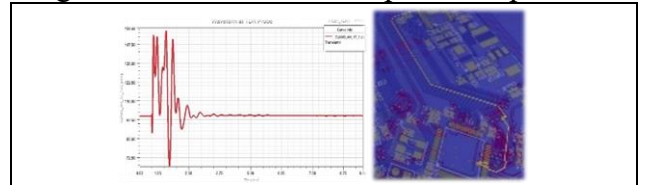
Figura 3.43 Traseele PWM M0_AH PWM analiza TDR (stânga), trasee (dreapta)
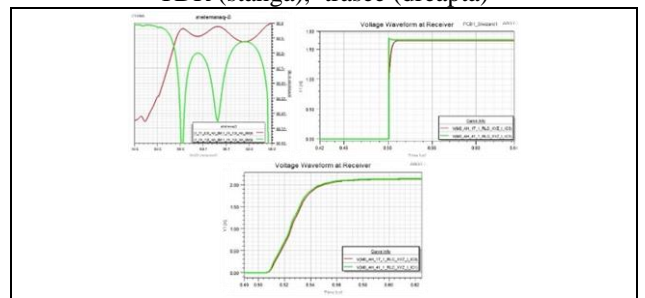
Figura 3.44 S-Parameter (stânga), semnal cu front rapid (mijloc), semnal cu front lent (dreapta)

The two cases presented are extreme scenarios: the fastest and slowest programmable rise times on the outputs, using IBIS data (Fig. 3.44).
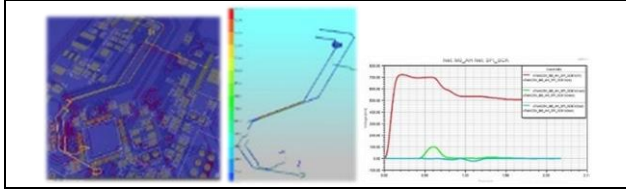
Figura 3.45 Crosstalk linie PWM - trasee (stânga), crosstalk overlay (mijloc), tensiune indusă (dreapta)

3.5.2 Fields Analysis
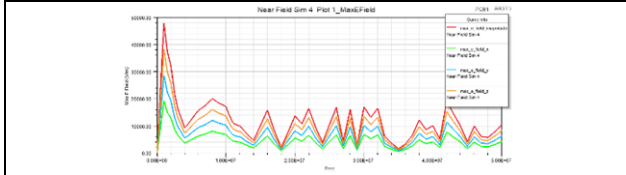
Figura 3.46 M0_AH – câmpul E
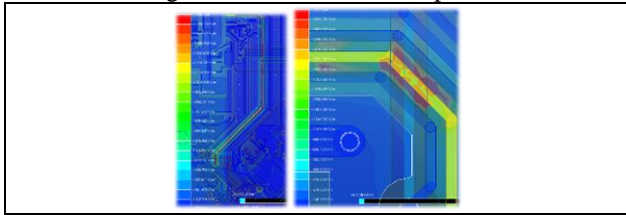
Figura 3.47 M0_AH câmpul E – reprezentare grafică și detaliu

The study of signals would not be complete without understanding the magnitude and distribution of electric and magnetic fields. The graph in Figure 3.46 shows the total electric field (E-field) along with the field distribution in the X, Y, and Z directions. Figure 3.47 provides additional visual cues regarding the distribution and magnitude of the electric field at its peak value along the signal path.
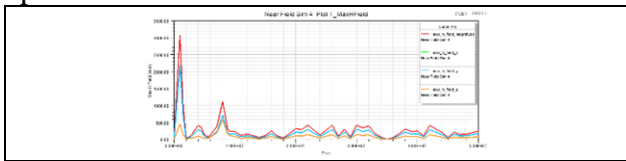
Figura 3.48 M0_AH – câmpul H
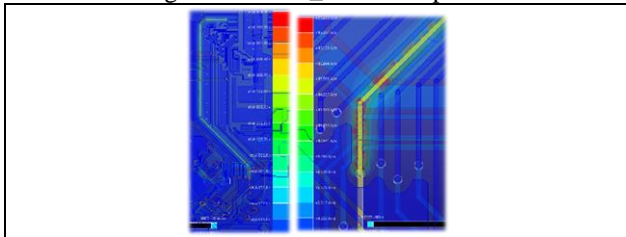
Figura 3.49 M0_AH câmpul H reprezentare grafică și detaliu

Figure 3.48 and Figure 3.49 visually depict the strong magnetic field generated around M0_AH at 1MHz..
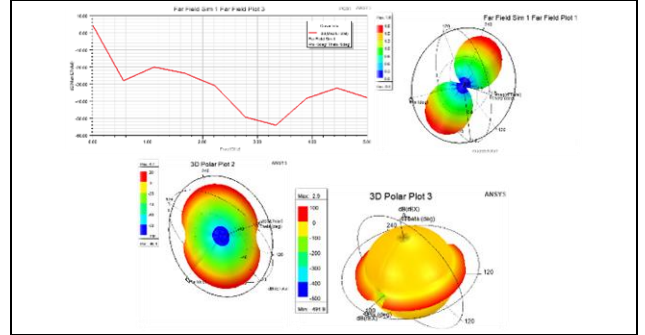
Figura 3.50 M0_AH Electromagnetic Far Field – mărime vs Frecventa (sus stânga); mărimea totală a câmpului (sus dreapta); mărimea totală polară (jos stânga); mărime polară X (jos dreapta)

Figure 3.50 presents the magnitude along the spatial axes.
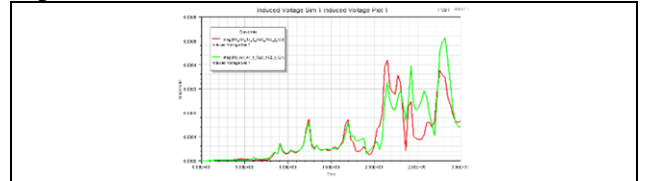
Figura 3.51 Impactul EMI extern asupra semnalului M0_AH

Figure 3.51 graphically identifies the induced voltage caused by a single incident electromagnetic field given by Phi=0deg, Theta=90deg, and polarization E0_Phi=0 and E0_Theta=1.
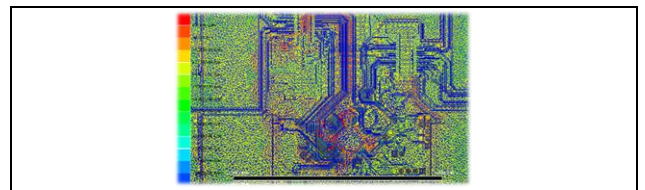
Figura 3.52 Câmpul J la 1MHZ

Figura 3.52 oferă un indiciu vizual asupra densității și orientării căilor de curent.

3.6 Conclusions

The current chapter has addressed the main steps taken by a designer to develop a printed circuit board. The components were initially placed guided by the thermal characteristics of major power-consuming components using Ansys IcePak. Then, the power network was analyzed, and decoupling and bypass capacitors were appropriately sized, while losses in the traces and power planes were determined using SiWave PI Advisor and

SiWave DC Analyzer. Signal integrity was studied using SiWave TDR Analyzer, S-Parameter Analyzer, Crosstalk Analyzer, and eye diagrams and transmission line characterization were determined using Ansys AEDT. Near and far fields were represented at significant frequencies along with the J field, and induced voltages due to external fields were analyzed using Ansys SiWave in combination with AEDT.

The analysis presented in this work was limited to a few representative traces and signals. It is understood that the rest of the board was approached in a similar manner to how analog and PWM signals were modeled and analyzed. Important insights were gained, leading to the discovery of several imperfections, such as USB trace impedance, crosstalk on analog feedback signals, and SPI interface speed, to name just a few. As a result, the solution was modified, and a new revision was issued. The design process heavily relied on powerful CAE software, such as ANSYS IcePak, SiWave, AEDT, and others, whose contribution was generally appreciated as remarkable.

Capitolul 4 – Compact vibration damping system

4.1 Introduction

Within this work, in addition to developing new solutions in linear technology, the field of vibration damping is also addressed in an attempt to propose a comprehensive technical solution capable of addressing a wide range of applications such as manufacturing machines, 3D printers, pick-and-place machines, Cartesian robots, machine tools, and more.

4.2 The study of the compression of thin air layers at the interface of the linear bearing

To derive the equations that describe the compression of a thin layer of air, the following parameters are idealized:

The thickness of the air layer is much smaller than the boundary surfaces.
The flow has a low velocity.
There is no vertical pressure gradient.
The horizontal flow follows a quadratic Poiseuille profile.
Air is modeled as an ideal gas, described by the ideal gas equation.
The system is isothermal, meaning that all heat generated by the system is immediately and completely absorbed by the environment.

System parameters:

η - *coefficient of dynamic viscosity*

$\xi - y/W$

α - $\alpha_n = \frac{h_0^2 P_0 n^2 \pi^2}{12 \eta W^2}$

σ - $\sqrt{\sigma_n} = n\pi$

ω_c - $\omega_C = \frac{\pi^2 h_0^2 P_0}{12 \eta W^2}$

τ – *shear stress*
ρ – *density*
P – *gas pressure*
V – *gas volume*
n – *molar mass of the gas*
h – *distance between the plates*
R – *universal gas constant= 8.3*103 [J/(kg*K)]*
T – *absolute temperature of the gas*
L – *characteristic length of the flow (from Reynolds number)*
U – *characteristic velocity of the flow (from Reynolds number)*
g – *gravitational acceleration*
x, y, z – *Cartesian directions*
K – *Knudsen number (ratio of mean free path (λ) to characteristic length h)*
(λ) și lungimea caracteristică h)
W – *width of the upper plate*

$$12\eta \frac{\partial(Ph)}{\partial t} = \nabla \cdot [(1 + 6K_n)h^3 P \nabla P] \qquad (4.1)$$

$$\frac{\partial(Ph)}{\partial t} = \frac{h^3}{12\eta} \nabla[P\nabla P] \Rightarrow \qquad (4.2)$$

$$\frac{\partial(Ph)}{\partial t} = \frac{h^3}{12\eta} \frac{1}{2} \nabla^2 P^2 \qquad (4.3)$$

$$h = h_0 + \delta h \quad unde \quad \delta h \ll h_0 \qquad (4.4)$$

$$P = P_0 + \delta P \quad unde \quad \delta P \ll P_0 \qquad (4.5)$$

The problem will be further simplified by considering a one-dimensional flow, which means that the pressure has a gradient only in one direction, chosen to be the y-direction, perpendicular to the length of the plates.

$$\frac{\partial((P_0 + \delta P)(h_0 + \delta h))}{\partial t} = \frac{(h_0 + \delta h)^3}{12\eta} \frac{1}{2} \frac{\partial^2 (P_0 + \delta P)^2}{\partial y^2} \qquad (4.6)$$

$$(h_0 + \delta h)\frac{\partial(\delta P)}{\partial t} + (P_0 + \delta P)\frac{\partial(\delta h)}{\partial t} = \frac{(h_0 + \delta h)^3}{12\eta}(P_0 + \delta P)\frac{\partial^2 \delta P}{\partial y^2} \qquad (4.7)$$

$$\frac{\partial \frac{\delta P}{P_0}}{\partial t} + \frac{\partial \frac{\delta h}{h_0}}{\partial t} \approx \frac{h_0^2 P_0}{12\eta} \frac{\partial^2 \frac{\delta P}{P_0}}{\partial y^2} \qquad (4.8)$$

We note:

$$\hat{p} = \frac{\delta P}{P_0} \tag{4.9}$$

$$\xi = \frac{y}{W} \tag{4.10}$$

so:

$$\frac{\partial \hat{p}}{\partial t} - \frac{h_0 P_0}{12\eta W^2} \frac{\partial^2 \delta \hat{p}}{\partial \xi^2} = -\frac{\dot{h}}{h_0} \tag{4.11}$$

The equation describing the pressure variation is now written in the form of a linear partial equation dependent on the plate velocity.

$$\frac{\partial \hat{p}}{\partial t} - \frac{h_0^2 P_0}{12\eta W^2} \frac{\partial^2 \delta \hat{p}}{\partial \xi^2} = 0 \tag{4.12}$$

The solutions are of the form:

$$\hat{p}(\xi, t) = \hat{p}(\xi) e^{-\alpha t} \tag{4.13}$$

By substituting the solution form into the equation:

$$\alpha \hat{p} + \frac{h_0^2 P_0}{12\eta W^2} \frac{\partial \hat{p}}{\partial \xi^2} = 0 \tag{4.14}$$

We derive the solutions from:

$$\hat{p} = A_n \sin(\sqrt{\sigma_n} \xi) + B_n \cos(\sqrt{\sigma n} \xi) \tag{4.15}$$

$$\sigma_n = \frac{12\eta W^2 \alpha_n}{h_0^2 P_0} \tag{4.16}$$

To simplify the solutions, let's assume that at the upper plate's edge, the pressure is equal to the ambient pressure P_0, or in other words, the pressure gradient in those regions is zero ($\hat{p} = 0$). Due to symmetry:

$$\frac{d\hat{p}}{d\xi} = 0 \ pentru \ \xi = \frac{1}{2} \tag{4.17}$$

So:

$B_n = 0$ for every n

$A_n = 0$ for every even n

$$\sqrt{\sigma_n} = n\pi \Rightarrow \alpha_n = \frac{h_0^2 P_0 n^2 \pi^2}{12\eta W^2} \ pentru \ n \ impar \tag{4.18}$$

The values of A_n for odd values of n can be identified from the condition that the plate moves uniformly relative to the lower plate.

$$A_n = -\frac{4z_0}{h_0 n\pi}; \quad pentru \ n \ impar \tag{4.19}$$

The full solution:

$$\hat{p} = -\frac{4z_0}{h_0 \pi} \Sigma \frac{1}{n} \sin(\sqrt{\sigma_n} \xi) e^{-\alpha_n t} \ , n \ impar \tag{4.20}$$

The total force acting on the plate is given by:

$$F(t) = \int_0^1 \delta p L \, dy = \int_0^1 \delta p L W \, d\xi \tag{4.21}$$

$$F(t) = P_0 W L \int_0^1 \hat{p}(t, \xi) \, d\xi = -P_0 W L \frac{4z_0}{\pi h_0} \int_0^1 \left(\Sigma \frac{1}{n} \sin(n\pi\xi) e^{-\alpha_n t} \right) d\xi \tag{4.22}$$

$$F(t) = -P_0 W L \frac{8z_0}{\pi^2 h_0} \Sigma \frac{1}{n^2} e^{-\alpha_n t}, n \ impar \tag{4.23}$$

The Laplace transform of the impulse response, from 0 to infinity, is (for odd n):

$$F(s) = -P_0 W L \frac{8z_0}{\pi^2 h_0} \Sigma \frac{1}{n^2} \frac{1}{s + \alpha_n} \tag{4.24}$$

$$F(s) = -P_0 W L \frac{8z_0}{\pi^2 h_0} \frac{12\eta W^2}{\pi^2 h_0^2 P_0} \Sigma \frac{1}{n^4} \frac{1}{\frac{s}{\alpha_n} + 1} \tag{4.25}$$

$$F(s) = -\frac{96\eta L W^3}{\pi^4 h_0^3} s \left(\frac{z_0}{s}\right) \Sigma \frac{1}{n^4} \frac{1}{\frac{5}{\alpha_n} + 1} \tag{4.26}$$

For an arbitrary velocity, the Laplace transform of the force is (velocity = z(s))

$$F(s) = -\frac{96\eta L W^3}{\pi^4 h_0^3} s \left(\frac{z_0}{s}\right) \left(\Sigma \frac{1}{n^4} \frac{1}{\frac{s}{\alpha_n} + 1} \right) s \cdot z(s) \tag{4.27}$$

From the above series, only the first term is of interest. The expression for the force then becomes:

$$F(s) = \frac{b}{1 + \frac{s}{\omega_c}} s \cdot z(s) \tag{4.28}$$

$$b = \frac{96\eta L W^3}{\pi^4 h_0^3} \tag{4.29}$$

$$\omega_c = \frac{\pi^2 h_0^2 P_0}{12\eta W^2} \tag{4.30}$$

Also of practical interest for integrating the device into the calculation of a larger system is the transfer function that relates the plate velocity to the force..

$$H(s) = \frac{F(s)}{s \cdot z(s)} = \frac{b}{1 + \frac{s}{\omega_c}} \tag{4.31}$$

It can be observed that the function has the form of a low-pass filter with a characteristic frequency ω_c.

$$H(s) = \frac{F(s)}{z(s)} = \frac{s \cdot b}{1 + \frac{s}{\omega_c}} \tag{4.32}$$

Although the above analytical development made certain simplifying assumptions, the result accurately anticipates the system's behavior. At low frequencies, the plate moves through the fluid at a slow velocity, allowing the fluid to flow outwards, resulting in damping. This damping is undoubtedly a dissipative action, which in this application is a beneficial phenomenon as it reduces the vibration amplitude. At high frequencies, the plate compresses the gas, creating a "gas spring" that stores potential energy. This spring reduces the plate's motion amplitude but does not directly dissipate energy. However, the transfer of energy from kinetic energy of the plate to potential energy in the compressed gas can only occur through a dissipative process, which again contributes to vibration damping..

4.3 Analytical study of the compression of magnetorheological thin liquid layers

The technology proposes a series of advantages that could lead to remarkable achievements:

The ability to generate very high damping forces in an extremely compact space with low mass.

The capacity to modify the mechanical impedance seen by vibrations, thus enhancing the ability to dissipate oscillatory energy over a wider spectrum and, as a direct consequence, the ability to break up standing wave maintenance. In this regard, there is already at least one patent [4] proposing a solution based on this technology.

The ability to generate small vibrations that can be used to break the contact in the adjacent linear sliding bearing, thus reducing its stick-slip behavior.

Semi-active or passive adaptive control.

The ability to change operating parameters with a bandwidth of up to 1kHz.

Cost efficiency.

Relatively low control energy compared to other technologies: inertial dampers, ER fluids, piezo systems.

Concentrated suspensions containing solid particles in Newtonian liquids demonstrate a threshold of effort, followed by Newtonian behavior. These types of liquids are commonly referred to as "Bingham plastic fluids" (Figure 4.1).

.

$$\tau = GB \quad pentru \ |\Pi_\tau| \le \tau_y^2 \qquad (4.33)$$

$$\tau = 2\left(\eta_0 + \frac{\tau_y}{2|\Pi|_{D^{1/2}}}\right)D \ pentru \ \left|\Pi_{\tau_y}\right| > \tau_{y0}^2 \qquad (4.34)$$

Here τ, D and B represent the internal stress, strain rate, and deformation tensors, respectively. G is the modulus of elasticity, and η_0 is the viscosity below the yield stress region. τ_y is the yield stress, and, Π_D is the second invariant of D.
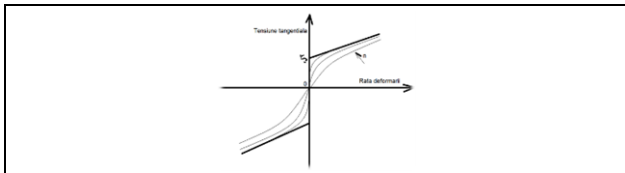
Figura 4.1 Fluid Bingham – funcție von Mises și aproximări Papanastasiou (varierea numărului n aduce funcția aproape de curba reală a fluidului)

In 1987, Papanastasiou and colleagues proposed another form of the equation, one that could describe both states using a single expression, namely:

$$\tau = -\left[\eta_0 + \frac{\tau_y(1 - e^{-n\dot\gamma})}{\dot\gamma}\right]\dot\gamma \qquad (4.35)$$

Where γ is the shear rate, and n is the regularization parameter that allows the function to conform to the actual stress-strain relationship of the fluid.

The solutions to this equation in the special case of magnetorheological fluids were solved by Alireza Farjoud [12] by generating the non-dimensional form, choosing:

$$v = \frac{-\dot h R}{h}, \qquad \dot\Gamma = \frac{\dot\gamma h}{V}, \qquad T = \frac{\tau}{\eta_0 V/h}, \qquad \varepsilon = \frac{h}{R} \qquad (4.36)$$

Where V is the characteristic velocity, τ is the stress tensor, $\dot\gamma$ is the strain rate tensor, $\dot\Gamma$ is the non-dimensional tensor of the strain tensor, and T is the non-dimensional tensor of stresses. The ratio between the radius and the distance between the plates is ε.

The Papanastasiou equation becomes in non-dimensional form:

$$T = -\left[1 + \frac{Bn(1 - e^{-N\dot\Gamma})}{\dot\Gamma}\right]\dot\Gamma \qquad (4.37)$$

where $B_n = \dfrac{\tau_y h}{V\eta_0}$ Bingham number, and

$N = \dfrac{n_v}{h}$ is the non-dimensional regularization of the parameter n in the Papanastasiou model..

4.4 Solution Draft
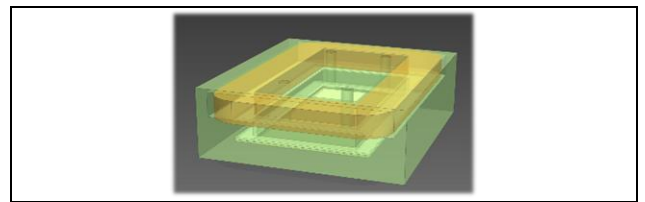
Fig. 2 Vedere de ansamblu al amortizorului

The proposed system (Fig. 3) consists of two bodies connected by flexure blades that guide the upper subassembly in its oscillatory motion along the z-axis. The body is composed of materials permeable to the electromagnetic field and has two air gap sections. The first section is occupied by the magnetorheological fluid and ensures a uniform distribution of the magnetic field, resulting in viscosity without significant gradients. The second section is necessary to separate the two bodies that are in relative motion to each other..
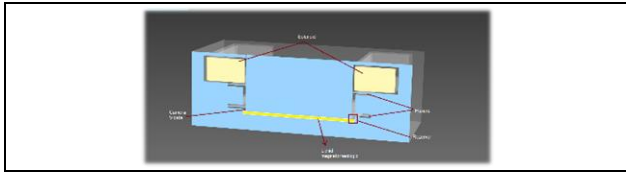
Fig. 3 Detaliu dispozitiv

The magnetorheological fluid is sealed in a vacuum environment to prevent contamination with gas bubbles, which can unpredictably affect its viscosity. It is not yet clear if this is absolutely necessary, and prototype tests will provide more data in this regard. During compression, the fluid will rise through the extremities towards a special zone where it can accumulate. The return from this zone is achieved through both decompressing the area when the upper body moves along the z-axis and gravitational forces..
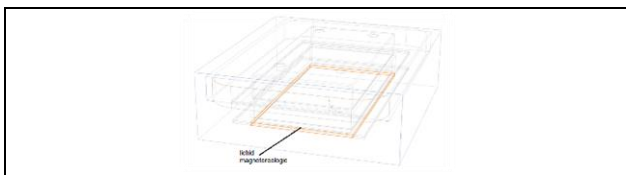
Fig. 4 Ansamblu complet cu identificarea poziției fluidului

4.5 Conclusions

Vibrations are a central issue in the context of production machines, especially in the case of machine tools. In this paper, the most important methods of treating vibrations have been reviewed. Among the possible technologies, two have been chosen. The first technology is the damping that occurs in thin fluid layers when subjected to compression and decompression. The second technology complements the first one synergistically. It is the technology of fluids controlled by electromagnetic fields. The choice was made due to the high damping capabilities it can achieve in a limited space and the wide frequency range in which it can be effective, primarily due to the properties of magnetorheological fluid. The paper presents the analytical foundations for constructing an active vibration damping system using the aforementioned technologies, as well as a mechanical solution sketch. The system has very promising characteristics, especially because it can be integrated into any solution as part of the axial bearing.

Capitolul 5- Sliding bearings and linear mechanisms

5.1 Experimental examples
5.1.1 Machine Tool bearing

Polymeric thrust bearing, constructed from ultra-high-density polyethylene, with a counterpart made of 1.4301 steel (SS304). It provides lubrication-free rolling, negligible stick-slip behavior, and good vibration damping.
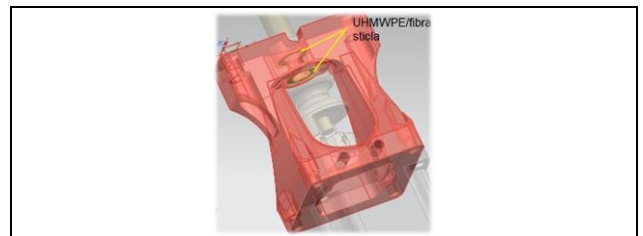
Figura 5.1 Lagăr Axa liniara mașină-unealtă

Figura 5.2 Lagăr mașină-unealtă - structură experimentală

5.1.2 Axial bearing for production machine

A linear motion system with a movable nut/nuts for fast multi-axis movements on the same lead screw with a nut, and an axial bearing made of polymer materials such as POM (Polyoxymethylene) and UHMWPE (Ultra-High Molecular Weight Polyethylene) reinforced with carbon fibers..
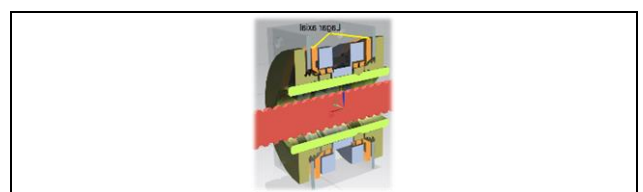
Figura 5.3 Lagăr axial polimeric

Figura 5.4 Ansamblu experimental șurub - piuliță

5.2 Linear axis draft solution

In the solution presented in this work, a trapezoidal screw with a 30-degree angle was chosen, despite the fact that square screws have higher efficiency. The arguments against choosing square screws were that they flex more at the base and are more costly. The second element on which the solution is based is the more uniform distribution of the nut flanks on the screw flanks by dividing the nut into smaller individually tensioned pieces. The solution presented in this work considers only two pretensioned pieces, but this technique can be used to create many such zones, even smaller than 360 degrees. In extreme cases, the nut can be divided into dozens of pieces, pretensioned in groups or individually, increasing the contact surface, ideally up to 100%.

As for the axial bearing of the transmission, it must meet several requirements:

It should be immune to chips/fine wood dust, adjustable to compensate for axial play and allow variation in rigidity by adjusting the pre-load.

It should have the ability to dampen vibrations.
It should require low maintenance.

It should be capable of efficiently and safely transferring mechanical energy.

The final solution includes a sliding axial bearing, consisting of a flat surface made of ultra-high molecular weight polyethylene (UHMWPE). This surface is threaded onto the main shaft in predetermined increments based on the geometry of the outer blade sections of the surface until it contacts the fixed part of the bearing and the desired pre-load is achieved. The geometry of the outer blade sections consists of a flexible part whose compliance is studied using the same principles as those of the flexure blades of the linear guide, as it exhibits the same physical phenomenon. At the end of each blade on the lower side, small cones are located, which find their place on the outer part of the shaft. With each rotation, the flexure blades index another hole on the shaft, allowing for pre-load variation or just compensation for play. These conical protrusions represent the main mechanism for transferring torque between the shaft and the bearing.
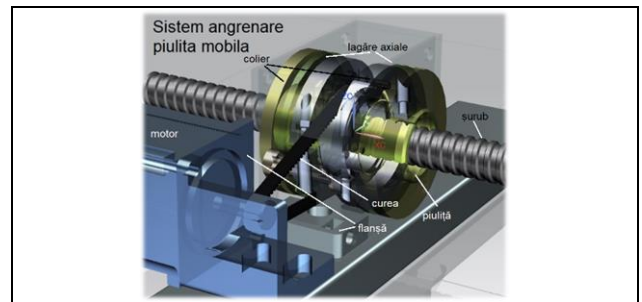
Figura 5.5 Schiță soluție a transmisiei liniare
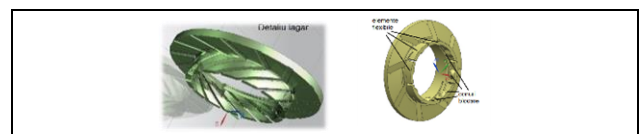
Figura 5.6 Lagăr axial, detalii părți componente
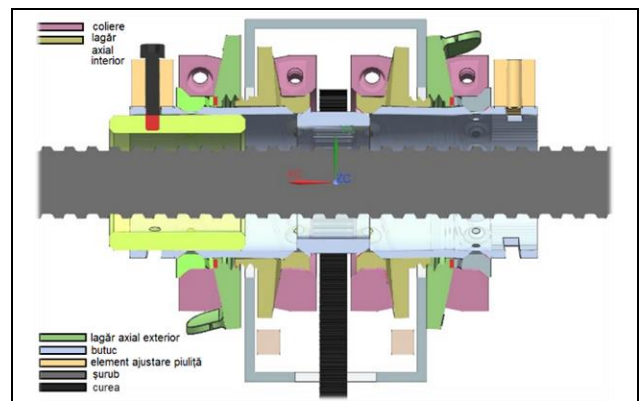
Figură 5.7 Secțiune plană prin transmisia șurub – piuliță

The transmission construction consists of the following components (Figure 5.7):
Axial bearing
Bearing clearance and pre-load adjustment system with threads
Adjustment system with integrated compliant blades within the bearing
UHMWPE/steel sliding coupling
Bearing fixation system
Locking cones
Counter-cones
Fixation collars
Rotational torque transfer system
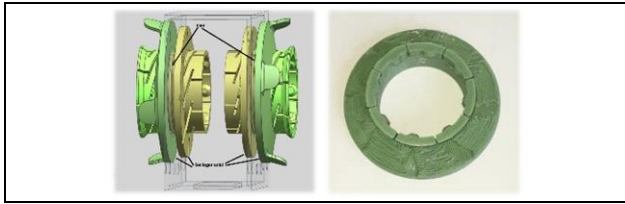
Figura 5.8 Set lagăr axial cu ajustare prin filet

The axial clearance adjustment and the variation of bearing stiffness are achieved by modifying the distance between the constructive elements (Figure 5.8) using a threaded system. The adjustment occurs in predefined increments. With each change in distance, the flexible blades, equipped with a series of locking cones at their edges, index the holes in the hub (Figure 5.9, Figure 5.8, and Figure 5.13).
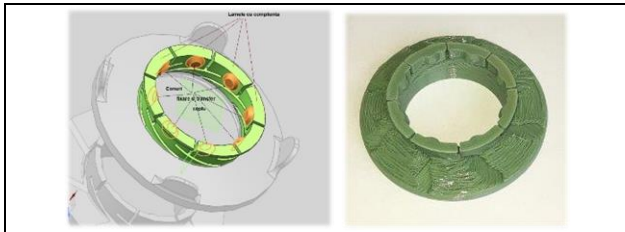
Figura 5.9 Conuri de fixare si de transfer cuplu

The cones have the freedom to exit the current hole due to the compliance of the blade on which they are located, allowing for flexing in two directions. The first direction is radial, allowing the cone to exit the hole, while the second direction is axial, allowing the bearing to move for adjustment (Figure 5.9 and Figure 5.10).).
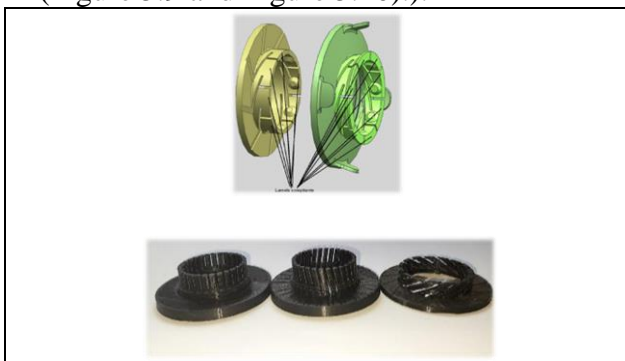
Figura 5.10 Sistem de ajustare axial realizat cu ajutorul lamelelor cu complianță; a) construcție finală; b) stagii evoluție formă

The conical shape of the locking pins allows for the elements of the system to be locked

without any clearance. Unlike cylindrical pins and holes, conical pins have the property of intrinsic adjustment due to their shape..
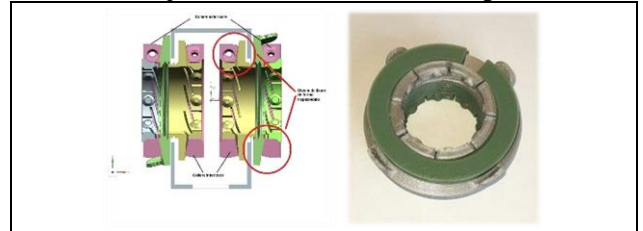
Figura 5.11 Sistem fixare lagăr realizat cu ajutorul colierelor cu profil trapezoidal

After adjustment, the moving elements of the bearing are locked using specially designed collars. The collars are tightened with screws, allowing for locking without the need for significant tightening torque. This is because the locking is not achieved through friction but through pin locking. By doing so, the possibility of creep, a sensitivity specific to polymer materials under mechanical loads, is eliminated (Figure 5.11)..
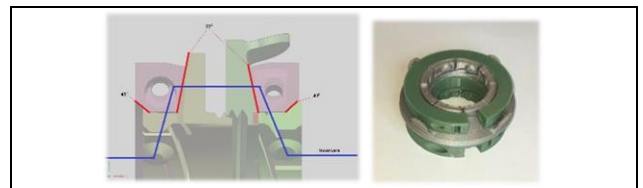
Figura 5.12 Detaliu profil trapezoidal si linia de forță

By ensuring proper contact angles between the collar and the two surfaces of the moving parts of the bearing, as well as the fastening elements, the transfer of torque from the hub to the bearing is facilitated without altering the position of the flexible blades. The tightening of the collar establishes a rigid mechanical system in conjunction with the blades and cones. This intentional design feature allows for torque transfer while protecting the blades, which, due to their compliance, cannot withstand the usual loads generated during operation alone (Figure 5.12).
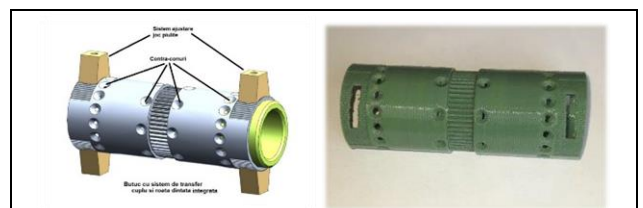
Figura 5.13 Butuc cu roata dințată integrată

The lower part of the system is represented by the hub. It connects the elements of the bearing, the two screw-nut systems, and the belt drive. The hub is equipped with two oblique slots and a graduated scale at its ends, allowing for external adjustment pieces mounted externally through a screw to modify the distance between the two drive nuts of the system by rotation, thus compensating for axial play (Figure 5.13).
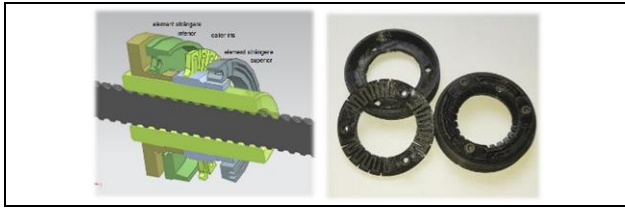
Figura 5.14 Varianta constructiva de tip iris
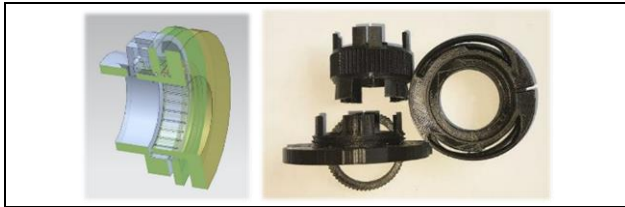
Figura 5.15 Varianta cu lamele verticale; stadiu incipient al soluției finale

The final design variant underwent several evolutionary iterations, one of which is presented in Figure 5.15. The hub was constructed from three pieces that interlocked through teeth with the moving parts of the bearing. The flexible blades were straight and did not have conical indentations. The collars were equipped with circular tightening straps to equalize pressures within the material and prevent creep of the polymer elements..

Screw-Nut transmission
Forces and Moments
The external loads applied to the transmission generate forces and moments.:

$$M_m = F_m * L \tag{5.4}$$

where Mm is the motor moment, Fm is the external force acting on the nut, and L is the force arm which, in the special case of this system, is the radius of the gear wheel integrated into the transmission.
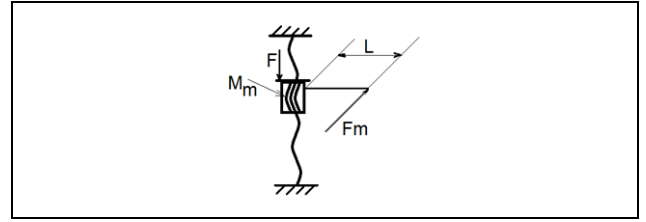
Figura 5.16 Forțe și momente în transmisie

The force F represents the axial force that represents the load to be moved. Under the action of this force, two resisting moments occur: the screwing moment that arises in the helical couple due to the friction between the threads, and the friction moment that occurs between the rotating nut and the supporting surface ([13]):

$$M_m = M_{insurubare} + M_f \tag{5.5}$$

$$M_{insurubare} = F\frac{d}{2}tg(\varphi + \beta) \tag{5.6}$$

Where d- is the diameter of the screw, β- is the average helix angle of the thread, and φ is the friction angle. In the current application case:

$$M_{insurubare} = 100N * 0.008m * tg(37°) \tag{5.7}$$

$$M_{insurubare} \cong 0.6 \, Nm \tag{5.8}$$

$$M_{insurubare} \cong 0.6 \, Nm \tag{5.9}$$

$$M_f = \frac{1}{3}\mu F\frac{d_c^3 - d_0^3}{d_c^2 - d_0^2} \tag{5.10}$$

Where d_c is the inner diameter of the nut, μ is the friction coefficient between the material of the nut and the material of the screw (UHMWPE/steel), and d_0 is the pitch diameter of the screw.

$$M_f = \frac{1}{3} * 0.15 * 100N\frac{(4096 - 1331)10^{-9}m^3}{(256 - 121)10^{-6}m^2} \tag{5.11}$$

$$M_f = 102 * 10^{-3}Nm \tag{5.12}$$

$$M_m = M_{insurubare} + M_f = 0.6Nm + 0.102Nm = 0.702Nm \tag{5.13}$$

5.3 Conclusions

This chapter deals with the development of a screw-nut drive system that meets the following requirements: it should be immune to wood chips/fine dust, adjustable to compensate for axial play and allow for stiffness variation by adjusting the preload, capable of damping vibrations, require low maintenance, and, last but not least, efficiently and safely transfer mechanical energy.

The final solution includes an axial sliding bearing consisting of a flat surface made of ultra-high molecular weight polyethylene (UHMWPE). This surface is threaded onto the main shaft in predetermined increments of the

outer blade geometry until it contacts the fixed part of the bearing and achieves the desired preload. The outer blade geometry comprises a flexible section. At the end of each blade on the lower side, small cones are present that fit into corresponding recesses on the outer surface of the shaft. With each rotation, the flexible

blades index to another hole in the shaft, allowing for preload variation or simply compensating for play. These conical protrusions represent the main mechanism for transferring torque between the shaft and the bearing.

Capitolul 6 – Dissemination of results, final conclusions, original contributions, and future research directions

6.1 Diseminarea rezultatelor

The research conducted during the doctoral thesis has materialized in the elaboration and publication of a total of 11 scientific articles, both in specialized journals and in conference proceedings, as follows:

Burducea, Sorin; Zapciu, Miron;   Direcții noi în sistemele de producție, aliniate cu filosofia "Industry 4.0" / New Principles Dictated by „Industry 4.0" în Factory Automation, Conferinta stiintifică a AOSR, 30 martie 2018, București, *https://www.aosr.ro/wp-content/uploads/2018/03/Program-conferin%C8%9B%C4%83-AOSR-30-martie-2018-DOAR-pe-sec%C8%9Biuni-1-1.pdf*

Burducea, Sorin; Zapciu, Miron;   Fluide magnetoreologice pentru controlul activ al vibrațiilor sistemelor mecanice; Conference Proceedings of the Academy of Romanian Scientists PRODUCTICA Scientific Session; altele; 25-27 May 2018; Online ISSN 2067-9564 Volume 10, Number 1/2018

Burducea, Sorin; Zapciu, Miron;   Advanced polymers used în plain bearings / Materiale polimerice avansate utilizate în construcția lagărelor de alunecare; Conference Proceedings of the Academy of Romanian Scientists PRODUCTICA Scientific Session; 29-30 May 2020

Burducea, Sorin; Zapciu, Miron;   Utilizarea structurilor cu design bionic la realizarea batiurilor mașinilor unelte; Politehnica București, catedra Ingineria sistemelor deproductie, curs an IV

Burducea, Sorin; Zapciu, Miron;   PCB Design of a Servo Motor Controller Under Strict Cost Constrains - PI Aware Design; International Journal of Innovative Research în Advanced Engineering, VIII, 335-343; doi: https://doi.org/10.26562/ijirae.2021.v0812.003

Burducea, Sorin; Zapciu, Miron;   Simulation technologies used în high-speed PCB design / Tehnologii digitale utilizate în elaborarea structurilor circuitelor imprimate de viteza mare din industria electronică; Conference Proceedings of the Academy of Romanian Scientists PRODUCTICA Scientific Session; 4 June 2021

Burducea, Sorin; Zapciu, Miron;   PCB Design of a Servo Motor Controller Under Strict Cost Constrains - Signal Integrity Aware Design; International Journal of Innovative Research în Advanced Engineering, VIII, 322-334; doi: https://doi.org/10.26562/ijirae.2021.v0812.005

Burducea, Sorin; Zapciu, Miron; PCB Design of a Servo Motor Controller Under Strict Cost Constrains - Thermal Aware Component Layout; International Journal of Innovative Research în Advanced Engineering, VIII, 335-343; doi: https://doi.org/10.26562/ijirae.2021.v0812.002

Burducea, Sorin; Zapciu, Miron; Ultra-flexible Business Models Empowered by Novel Furniture Production"; IBIMA 39th Internatial Conference, Granada, Spain, 30-31 May (ISBN: 978-0-9998551-8-8) (ISSN: 2767-9640).

Burducea, Sorin; Zapciu, Miron; Economical high robustness and precision linear guide / Ghidaj linear economic cu robustețe și precizie ridicate;
PRODUCTICA 2022, Conference Proceedings of the Academy of Romanian Scientists, Vol. 14, Nr.1/2022, ISSN 2067-2160 / Annals of AOSR, Series on Engineering, indexat DOAJ de ISSN Print 2066 – 6950; ISSN Online 2066 – 8570; http://aos.ro/editura/analeleaosr/annals-on-engineering; DOI:10.56082/annalsarscieng.2022.1.24

Burducea, Sorin; Zapciu, Miron; Flexure based linear guide with micrometric precision / Ghidaj liniar cu precizie micrometrică, bazat pe complianța materialelor;
PRODUCTICA 2023, To be publised - Under review –

6.2 Overall thessis conclusions

New production systems based on the concepts of Industry 4.0 attempt to bring a new vision on how technological processes interact with logistic procurement systems, how raw materials are processed, assembled, stored, and delivered. These new production systems enable the emergence of more flexible and efficient business models compared to traditional ones. The ultimate goal is to achieve individualized mass production, which promises long-term success in the market by catering to the new desires of customers and staying one step ahead of competitors who rely on conventional technologies.

The central focus of this work is to determine the feasibility of such a production system by identifying the conditions under which it could exist and finding hardware solutions that enable its creation. As a specific starting point, the paper considers an innovative production system applicable in the furniture industry. The new production system aims, among other things, to be characterized by portability through the provision of easy transportation directly to the site, user-friendliness through the full integration of all technological processes required for furniture production, zero maintenance during operation, and low cost. To meet the requirements of such a production system, among a range of possible situations and solutions, the paper identifies a set of circumstances in which the requirements can be met and explores potential mechanical and electronic solutions that can successfully assist in the creation of such a production system.

The circumstances identified in the research by the paper were defined as follows: to cover the system's portability aspect, if the system has a reduced mass and size, maximum two cubic meters and 400 kg, to allow transportation by regular road means, the system must consist of lightweight and cost-effective elements such as polymer materials, metal profiles, composite materials, and high power density motors like brushless servo motors. Under these circumstances, compared to a conventional production system, the new system can be much lighter, more flexible, and more cost-efficient. Polymer materials have been extensively studied in Chapter V, and as a result of this study, two materials with exceptional properties have been chosen for this application: polyoxymethylene, used for large-volume parts, and ultra-high molecular weight polyethylene (UHMWPE) for small-volume parts cut from sheets. Both materials exhibit good stability with temperature and humidity,

are self-lubricating, require no maintenance, can operate in highly contaminated environments with powders, have low creep, and demonstrate very high wear resistance. The use of polymer materials for numerous machine components instead of metal materials reduces the lifespan. It is known that the lifespan of technological systems is continuously decreasing, largely due to rapid advancements in manufacturing technologies and the need for continuous modernization. The lifespan of conventional production systems is approximately 20 years. Such longevity is no longer necessary in the current context due to the rapid moral depreciation of equipment. This paper demonstrates that a lifespan of only five years brings numerous benefits: up to 10 times reduction in costs and mass by replacing expensive and heavy metal materials with inexpensive and lightweight polymer materials..

The solutions identified through the research include the following sub-assemblies: linear guidance system, electronic drive system, vibration damping system, bearings, and screw-nut drive system. Regarding the linear guidance system, considering the premise of a cost-effective, accurate, lightweight, and low-maintenance system, the research has led to the creation of an innovative system composed of multiple arms connected by angular joints. The achieved performance is as follows:

Low cost: approximately €35 for the polymer version, €45 for the metal profile version, €120 for the epoxy granite version.

Accuracy: precision and repeatability are directly related to the bending stiffness differences of the blades forming the joints. By simply adjusting the width of the harder blades through polishing after assembly, the desired precision performance can be achieved. Angular deviations can be easily checked using a laser pointer against a wall at a distance of a few meters.

The weight of the guidance system varies depending on the construction as follows: polymer construction: 1.4 kg, metal profile construction: 2.1 kg, epoxy granite construction: 9.7 kg. For reference, a classic cast iron guide with similar characteristics weighs approximately 17 kg.

The system does not contain maintenance-requiring elements. For reference, a classic system may require bearing maintenance at short intervals, as short as a few months.

The lifespan is approximately 150,000 operating hours when using spring steel blades, with the lifespan dependent on the blades' ability to withstand repeated bending.

Regarding the electronic drive system, the paper addressed the main steps followed by a designer to develop a printed circuit board. The components were first placed guided by the thermal characteristics of major power-consuming components using Ansys IcePak. Then, the power network was analyzed, decoupling and bypass capacitors were properly sized, and losses in traces and power planes were determined using SiWave PI Advisor and SiWave DC Analyzer. Signal integrity was studied using SiWave TDR Analyzer, S-Parameter Analyzer, Crosstalk Analyzer, and Eye Diagrams and Transmission Line Characterization were determined using Ansys AEDT. Near and Far fields were represented at the most significant frequencies along with the J-Field, as well as induced voltages due to external fields using Ansys SiWave in combination with AEDT. The analysis presented in this paper was limited to a few representative traces and signals. It is understood that the rest of the board was approached in the same manner as the modeled and analyzed analog and PWM signals. Important insights were gained, leading to the discovery of multiple issues such as USB trace impedance, crosstalk on analog feedback signals, and SPI interface speed, to name just a few. The design was modified accordingly, and a new revision was issued. The design process relied heavily on powerful CAE software, such as ANSYS IcePak, SiWave, AEDT, and others, whose contribution was generally appreciated as remarkable.

The key objectives of the electronic system have been achieved. The system manages to meet the reliability and performance requirements using conventional manufacturing technology, which does not involve the use of advanced manufacturing technologies. This brings significant cost reductions and the possibility of manufacturing the PCB (Printed Circuit Board) in any location in Europe and not limited to just seven countries. This allows avoiding manufacturing the system in Asia without incurring any cost penalties.

Vibrations are a central concern in the context of production machinery, especially machine tools. This paper reviews the most important methods for addressing them. Among the possible technologies, two have been chosen. The first technology is that of damping, which occurs in thin layers of fluid when subjected to compression and decompression. The second technology complements the first one synergistically. It involves the use of fluids controlled by electromagnetic fields. The choice was made due to the significant damping that can be achieved in a limited space and the wide frequency range in which it can be effective, primarily due to the properties of the magnetorheological fluid. The paper presents the analytical foundations for constructing an active vibration damping system using the aforementioned technologies, as well as a mechanical solution outline. The system has very promising characteristics, especially because it can be integrated into any design as part of the axial bearing.

In its entirety, the paper answers the questions posed at the beginning, namely:

Is the existence of a production machine that is 10 times more cost-efficient than a conventional machine feasible, with functionality guided by the requirements of Industry 4.0 and capable of meeting the flexibility demands of mass production of customized products?
Under what circumstances is the existence of the machine feasible?
What solutions could be used?

The answer to the questions is: Yes, the existence of such a production machine is feasible, considering primarily the replacement of traditional materials (such as cast iron and steel plates) with polymers, metal profiles, and epoxy granite, as well as reducing the machine's lifespan from 20 years to only 5 years. The solutions are based on innovative designs that propose miniaturization and cost reduction through the use of materials and manufacturing processes with an excellent performance-to-cost ratio. The lack of system stability is compensated by rigid metal profile systems coupled with active vibration damping systems.

The solutions in this paper follow the same path that the electronics industry took more than 20 years ago when it decided to replace expensive and heavy materials such as copper with complex but inexpensive and lightweight control systems, despite significantly reduced lifespan. An eloquent example is voltage sources. Traditionally, they consisted of a voltage transformer, a rectifier bridge, and a low-pass filter. The transformer was heavy and expensive but had a lifespan of decades. These types of voltage sources, although extremely robust, are no longer available on the market today. They have been replaced by "switching" sources, much more complex electronic systems that compensate for the absence of the traditional transformer by using a transformer tens of times smaller and high-frequency control electronics. The market has decided that the second solution is the winner due to significantly lower cost, even though robustness is reduced by tens of times.

Once again, it is shown that the unbeatable force governing the market is price, and that is why the systems and philosophy presented in this paper will have a significant impact on the development of future production systems.

6.3   Original Contributions
- Within the thesis, mechanical and electrical solutions applicable to a linear axis for modern production machines are investigated. The mechanical solution is based on an innovative linear system coupled with a specially designed servo system to maximize cost efficiency and performance. All design elements, as well as the analysis and development of the system, represent the author's personal contributions, developed over 4 years of research, including:

- Determination of the kinematic operating concept consisting of two articulated arms and a movable carriage.
- Determination of the defining parameters of the kinematic concept, including the optimal relationship between the lengths of the arms (A = B) and the optimal relationship between the angles of the arms ($\alpha 1 = 2\ \alpha 2$).
- Identification of the functions underlying the determination of parameters that define the static and dynamic behavior of the system, such as the relationship between the width and length of an individual arm segment, the relationship between the angles of the flexible blades (angles of 30, 60, 90, and 120 degrees were studied), the length of the flexible blades (optimal at 50 cm), determination of analytical functions for static and dynamic deformation, FEM simulation of virtual models under static and dynamic deformation conditions.
- Determination of the optimal angle between the blades of the joint (120 degrees).
- Determination of the optimal dimensions of the joint blades (50x20x0.5-1 mm).
- Determination of the ways in which the mechanical system can be modified to cover a wide range of applications, including:
- Precision axes subjected to sustained vibrations, high loads, and low travel speeds (e.g., machine tools): identification of the four-arm solution, research on behavior using FEM simulations and experimental prototypes.
- Precision axes not subjected to sustained vibrations, with high travel speeds and low loads (e.g., pick-and-place, printer, etc.): identification of the two-arm solution and research on static and dynamic behavior using FEM simulations.
- Determination of the types of materials that can be used based on budget, mass, and application:
- Low budget, low mass, low rigidity (fast axes): determination of suitable polymer materials.
- Low budget, low mass, medium rigidity: determination of suitable metal profile types.
- High budget, medium mass, high rigidity: determination of the appropriate epoxy granite type and manufacturing methods.
- Determination of the optimal shape of the arms based on material, manufacturing techniques, and application.
- Determination of the optimal active vibration damping technology (SFD).
- Determination of the most efficient analytical analysis methods for the damping system (concentrated mass method).
- Determination of optimal solutions for passive vibration damping (large contact surfaces, etc.).
- Determination of the optimal type of fluid for the SFD system (fine iron filings, synthetic oil).
- Determination of solutions to eliminate the problem of air bubbles in the magnetorheological fluid (encapsulated system with integrated axial bearing).
- Investigation of the impact of dimensional parameters on the damping capacity.
- Determination of the possibility of breaking stick-slip by generating vibrations.
- Outlining a solution for active vibration damping.
- Processing and modification of the original ODrive electronic scheme.
- Calculation of LDOs, current consumption, and sizing of the power supply system.
- Determination of the power consumed by the microprocessor system.
- Determination of the power consumed by the DC-Bus system by identifying the frequency ranges involved and the amount of energy delivered by each capacitor through the development of an equivalent principle scheme and simulation in ANSYS AEDT under different load and discharge conditions.
- Determination of the power consumed by the power elements, MOSFETs, and feedback resistors.

- Determination of the power consumed by the three-phase drivers and calculation of powers by accumulating subsystems: inputs, output buffers, buck regulator, internal LDO, internal logic.
- Determination of the optimal thermal via type for double-sided FR4 PCB.
- Identification of thermal characteristics and simulation of heat distribution in the microprocessor circuit on FR4 substrate with two 1oz layers, including determination of convection currents.
- Identification of thermal characteristics and simulation of heat distribution in the three-phase driver circuits on FR4 substrate with two 1oz layers in two specific cases: without thermal vias and with thermal vias, including determination of convection currents.
- Identification of thermal characteristics and simulation of heat distribution in the LDO circuit on FR4 substrate with two 1oz layers.
- Identification of thermal characteristics and simulation of heat distribution in the DC-Bus circuit on FR4 substrate with two 1oz layers, without thermal vias, and determination of convection currents.
- Identification of thermal characteristics and simulation of heat distribution in the MOSFET and feedback resistor power circuit on FR4 substrate with two 1oz layers in two specific cases: without thermal vias and with thermal vias, including determination of convection currents.
- Simulation of heat distribution throughout the entire board and determination of areas exceeding the maximum load for the first solution variant.
- Identification of heat distribution throughout the entire board and determination of areas exceeding the maximum load through forced ventilation.
- Identification of heat distribution throughout the entire board and reduction of temperature ranges through the application of radiators.
- Simulation of heat distribution throughout the entire board and determination of areas exceeding the maximum load for the second solution variant.
- Routing of the entire board, over 1200 signals, in accordance with the determined placement in the previous step, consideration of current flows on each signal line, signal speed, reduction of cross-over, uninterrupted current lines, especially high-speed and analog lines, input and output buffer impedance, and maximum allowable line voltage drop; two major iterations and over 50 alternative variants were made.
- Analysis of voltage distribution: DCIR analysis and maximum voltage drops on the 3.3V power line; identification of the bias for the analog part of the two three-phase drivers.
- Determination of the cutoff frequency.
- Determination of the noise limit.
- Determination of the target impedance.
- Plotting the target impedance versus the solution from the schematic.
- Analytical determination of bulk capacitance.
- Determination of VRM impedance with and without
-
- determining how the bearing can meet the requirement for play compensation and preload variation (threaded system, compliant blades, locking cones, and axial indexing).

Regarding the electronic part, the current work has encompassed the complete development of the printed circuit board. This solution is entirely original and belongs solely to the author of the work. The development took one year and three months and went through two major iterations.

The components were initially placed guided by the thermal characteristics of the major power-consuming components using Ansys IcePak. Then, the power network was analyzed, and the decoupling and bypass capacitors were properly sized, while the losses in the traces and power planes were determined using SiWave PI Advisor and SiWave DC Analyzer. Signal integrity was studied

using SiWave TDR Analyzer, S-Parameter Analyzer, Crosstalk Analyzer, and Eye Diagrams and Transmission Line Characterization were determined with the help of Ansys AEDT. Near and Far fields were represented at the most significant frequencies, along with the J-Field, as well as the induced voltages due to external fields using Ansys SiWave in conjunction with AEDT.

The vibration damping system is part of a class of systems that is very sparsely documented in the specialized literature and represents a central innovative element of the work. The system proposes the use of a digitally controlled fluid with magnetic properties to achieve the dynamic values required by the application. This system is original and entirely developed by the author. As a complex mechatronic system, its final design has not been finalized yet. The developed solution is still in the sketch stage.

The design process relied heavily on powerful and state-of-the-art CAD/CAE software such as Siemens NX, Nastran, ANSYS IcePak, SiWave, AEDT, and others, without which the author could not have developed such a large-scale project in such a short time, demonstrating, if necessary, the effectiveness of modern design-assisted systems. The design was based on over 200 analyses and simulations, and therefore, the contribution of these systems was generally regarded as remarkable..

6.4   Future Research Directions

This paper presents the concepts on which future production systems can be based. Building upon these concepts, the following research directions include the development of numerous industrial applications, such as integrated machine tools, Cartesian robots, pick-and-place machines, printers, material handling, etc. At the subassembly level, the elements detailed in the paper require additional attention to reach a final stage of development and transition from the realm of research to production. Specifically:

Linear guidance:
Research on improving the maximum angles of the joints.
Research on enhancing the ratio between volume and useful stroke.
Research on improving the rigidity of the joints.
Research on implementing an adaptive system that independently modifies the angle of the arms based on the load direction.
Servo drive system:
Research on ways the system can be used with minor modifications to drive three-phase asynchronous motors.
Research on methods to anticipate a failure situation by considering the defect rates of each electronic element and its load over time.
Sliding bearings and linear transmission:
Research on integrating the servo motor directly into the nut-mobile system, thereby increasing rigidity and precision while reducing costs, size, and the number of components.
Integration of axial and radial bearings.
Vibration damping system:
Research on the influence of compression surface size on overall damping produced by the device and the frequency spectrum covered.
Production of an experimental system.
Research on an electronic control system.
Investigation of sensor types that can be used for feedback.

Bibliography

[1] Jorg Sydow & Markus Helfen, *Production as a service*. Berlin: Friedrich-Ebert-Stiftung, 2016.

[2] Elmo de Angelis, Kylene de Angelis, Mojca Vucovič, Gabriela Vlckova,Evanthia Batzogianni, Stella Ioannou Ludmiła Walaszczyk, *Business Models – compendium*. Radom: Publishing House of the Institute for Sustainable Technologies – National Research Institute, 2000.

[3] Larry Howell, *Compliant Mechanisms*.: Wiley-Interscience, 2001.

[4] Jonathan Hopkins and ML Culpepper, "Synthesis of multi-degree of freedom, parallel flexure system concepts via freedom and constraint topology (FACT)," *Precision Engineering*, 2010.

[5] M. Grubler, *Getriebelehre: eine Theorie des Zwanglaufes und der ebenen Mechanismen*. Berlin: Springer, 1917.

[6] Dana Silaghi-Perju, *Rezistenta Materialelor - Teorie si aplicatii*. Timisoara: Politehnica Timisoara.

[7] Mircea Rades, *Vibratii mecanice*. Bucuresti: Printech, 2006.

[8] Larry Howell and Brian Jensen, "The modeling of cross-axis flexural pivots," *Pergamon Press*, 2002.

[9] Marcel Thomas. (2017, Feb,) MIT Web. [Online]. http://web.mit.edu/mact/www/Blog/Flexures/FlexureIndex.html#DOF

[10] Ph.D., Matin graham, Ph.D. Howard W. Johnson, *High-Speed Digital Design - A handbook of Black Magic*.: Prentice Hall PTR, 1993.

[11] Atar - Sierra CIrcuits Mittal. (2020, Aug.) What is Power Integrity and Power Distribution Network? [Online]. https://www.protoexpress.com/blog/power-integrity-pdn-and-decoupling-capacitors/

[12] NIMA MAHMOODI, MEHDI AHMADIAN ALIREZA FARJOUD, *NONLINEAR MODEL OF SQUEEZE FLOW OF FLUIDS WITH YIELD STRESS USING PERTURBATION TECHNIQUES*.: Modern Physics Letters B Vol. 26, No. 7, 1150040, 2012.

[13] Dorina Matlesan, Teodor Madarasan, Dumitru Pop Alexandru Chisiu, *Organe de masini*. Bucuresti: Editura didactica si pedagogica, 1976.

[14] X. Xu and C. Zeng, *Design of a magneto-rheological fluid clutch based on electromagnetic finite element analysis*.: Computer Engineering and Technology (ICCET), 2010 2nd International Conference on, vol. 5, pp. V5–182, IEEE, 2010.

[15] W. M. Winslow, *Method and means for translating electrical impulses into mechanical force*.: US Patent 2,417,850, Mar. 25 1947.

[16] W.Kordonsky, *Magnetorheological as a base of new devices and technologies*.: Journal of Magnetism and Magnetic Materials, vol. 122, no. 1, pp. 395–398, 1993.

[17] W. E. Armstrong and F. E. Filisko, *Electric field dependent fluids*.: US Patent 4,744,914, May 17 1988.

[18] W. Beltman, *Viscothermal wave propagation including acousto-elastic interaction*.: Journal of Sound and Vibration 227, 555–586, 1999.

[19] N. Ohlson, M. Nilsson V. Noresson, *Design of electrorheological dampers by means of finite element analysis: theory and applications*.: Materials and Design 23, 361–369, 2002.

[20] T. Ohyama, K. Fujii T. Wakahara, *Suppression of wind-induced vibration of a tall building using tuned liquid damper*.: Journal of Wind Engineering and Industrial Aerodynamics 43, 1895–1906, 1992.

[21] N. Saga, and T. Nakamura, *Impedance control of a single shaft-type clutch using homogeneous lectrorheological fluid*.: Journal of intelligent material systems and structures, vol. 13, no. 7-8, pp. 465–469, 2002.

[22] Y. Saito T. Koizumi, *The damping capacity of a flat surface to roller contact*.: Wear 63, 347–357, 1980.

[23] Singiresu S. Rao, *Mechanical vibrations - 5th edition*.: University of Miami, Prentice Hall, 2011.

[24] Siemens PLM. (2016) NX Nastran 11 Release Guide.

[25] Siemens PLM. (2014) Nx Nastran User's guide.

[26] Siemens PLM. (2014) NX Nastran Quick Reference Guide.

[27] Siemens PLM. (2014) NX NAstran Numerical Methods Users's guide.

[28] ∗, Wenhua Yea, Peihuang Loua, Weifang Chena, Jungui Huangb and Lili Xiaoa Shihao Liua, *Bionic design for column of gantry machining center to improve the static and dynamic performance*. Nanjing : Jiangsu Key Laboratory of Precision and Micro-Manufacturing Technology, 2011.

[29] R. W. Phillips, *Engineering applications of fluids with a variable yield stress*.: PhD thesis, University of California Berkeley, 1969.

[30] R. Mangiarotty, *Acoustic radiation damping of vibrating structures*.: The Journal of the Acoustical Society of America 35, 369–377, 1963.

[31] R. Ehrgott and S. Masri, *Modeling the oscillatory dynamic behaviour of electrorheological materials in shear*.: Smart Materials and Structures, vol. 1, no. 4, p. 275, 1992.

[32] A. S. Shafer, and M. R. Kermani P. Yadmellat, *Design and development of a singlemotor, two-dof, safe manipulator*.: Mechatronics, IEEE/ASME Transactions on. 19. 1384-1391. 10.1109, 2014.

[33] Prof. Philippe Bocher, Alessandro MARRA Prof. Matteo Strano, *Vibration damping and cyclic loading of aluminum foam filled tubes*.: Politechnic Institute of Mainland, 2014.

[34] O. Reynolds, *On the theory of lubrication and its application*.: Philos. Trans. R. Soc. 177, 157–234.

[35] Oliver Romberg, *Passive damping device for sandwich structures*. Bremen: Deutsches Zentrum für Luft- und Raumfahrt (DLR), 2010.

[36] J. Furusho, and Y. Kiyota N. Takesue, *Fast response mr-fluid actuator*.: JSME International Journal Series C, vol. 47, pp. 783–791, 2004.

[37] H. Asaoka, J. Lin, M. Sakaguchi, G. Zhang, and J. Furusho N. Takesue, *Development and experiments of actuator using mr fluid*.: ndustrial Electronics Society, IECON 2000, 26th Annual Confjerence of the IEEE, vol. 3, pp. 1838–1843, IEEE, 2000.

[38] D. J. Romstadt, M. B. Lizell, and T. R. Weyenberg, N. K. Petek, *Demonstration of an automotive semi-active suspension using electrorheological fluid*.: SAE PUBLICATION SP 1074. NEW DEVELOPMENTS IN VEHICLE DYNAMICS, SIMULATION, AND SUSPENSION SYSTEMS (SAE TECHNICAL PAPER 950586), 1995.

[39] N. K. Petek, *An electronically controlled shock absorber using electrorheological fluid*.: tech. rep., SAE Technical Paper, 1992.

[40] W. PAWŁOWSKI, Ł. KACZMAREK N. KEPCZAK, *Cast iron and mineral cast applied for machine tool bed – dynamic behaviour analysis*.: Archives of Metalurgy and Materials, 2015.

[41] Y. Fujino, P. Warnitchai N. Hoang, *Optimal tuned mass damper for seismic applications and practical design formulas*.: Engineering Structures 30, 707–715, 2008.

[42] X.Wu, and J.Wong M. Sturk, *Development and evaluation of a high voltage supply unit for electrorheological fluid dampers*.: Vehicle System Dynamics, vol. 24, no. 2, pp. 101–121, 1995.

[43] J. Furusho, and N. Takesue M. Sakaguchi, *Passive force display using er brakes and its control experiments*.: Passive force display using er brakes and its control experiments, 2001.

[44] J. W. Bender, and J. D. Carlson M. R. Jolly, *Properties and applications of commercial magnetorheological fluids*.: 5th Annual International Symposium on Smart Structures and Materials, pp. 262–275, International Society for Optics and Photonics, 1998.

[45] N. Roitman, C. Magluta M. Louroza, *Vibration reduction using passive absorption system with Coulomb damping*.: Mechanical Systems and Signal Processing 19, 537–549, 2005.

[46] L. J. Hyde, G. M. Robinson, W. Ahmed M. J. Jackson, *Finite Element Analysis of Desktop Machine Tools for Micromachining Applications*.: ISBN: 978-953-51-0474-2, 2012.

[47] H. Numakura, M. Wuttig M. Ishimoto, *Magnetoelastic damping in Fe-Ga solid-solution alloys*.: Materials Science and Engineering: A 442, 195–198. Proceedings of the 14th International Conference on Internal Friction and Mechanical Spectroscopy, 2006.

[48] Mehmet Murat Altuğ Biçak, *Analytical investigation of squeeze film dampers*.: Michigan Technological University, 2011.

[49] H. Belek, A. Goksenli M. Bicak, *Vibration damping of a new ionic liquid under electric field effect*.: Acta Polytechnica 45, 68–72, 2005.

[50] Massalas, *Thermoelastic vibrations of a semi-infinite strip*.: Journal of Sound and Vibration 104, 337–341, 1986.

[51] R. Talipov, A. Kazakov, G. Stepanov L. Nikitin, *Mechanical and magnetic properties of polydisperse magnetoelastics*.: Solid State Phenomena 152-153, 155–158, 2009.

[52] Reckmann H, Popp K, Romberg O Kroeger M, *Friction strip damping in lightweight structures*.: Soc Appl Math Mech Padua, 2003.

[53] K. Park K. Lee, *Optimal robust control of a contactless brake system using an Eddy current*.: Mechatronics 9, 615–631, 1999.

[54] Klamt K., *Optimization of vibration damping due to joint patch friction in structures*. Duesseldorf : Prog Rep VDI 11th ed. No. 134, 1990.

[55] T. G. Duclos, J. D. Carlson, M. J. Chrzan, and A. J. Margida K. D. Weiss, *High strength magneto-and electro-rheological fluids*.: tech. rep., SAE Technical Paper, 1993.

[56] J. Rabinow, *Rabinow*.: Nov. 20 1951. US Patent 2,575,360, 1951.

[57] J. Rabinow, *The magnetic fluid clutch*.: Electrical Engineering, vol. 67, no. 12, pp. 1167–1167, 1948.

[58] J. D. Carlson and M. J. Chrzan, *Magnetorheological fluid dampers*.: US Patent 5,277,281, 1994.

[59] J. D. Carlson, *Electrorheological fluids*.: US Patent 4,772,407, Sept. 20 1988.

[60] J. D. Carlson, *What makes a good mr fluid?*: Journal of Intelligent Material Systems and Structures, vol. 13, no. 7-8, pp. 431–435, 2002.

[61] J. Chen and W. Liao, *Design, testing and control of a magnetorheological actuator for assistive knee braces*.: Smart Materials and Structures, vol. 19, no. 3, p. 035029, 2010.

[62] J. Chen andW.-H. Liao, *Design and control of a magnetorheological actuator for leg exoskeleton*.: Robotics and Biomimetics, 2007. ROBIO 2007. IEEE International Conference on, pp. 1388–1393, IEEE, 2007.

[63] D. Catanzarite, and K. St. Clair J. Carlson, *Commercial magneto-rheological fluid devices*.: International Journal of Modern Physics B, vol. 10, no. 23n24, pp. 2857– 2865, 1996.

[64] J. Carlson and B. Spencer Jr, *Magneto-rheological fluid dampers for semi-active seismic control*.: Proc. of the 3rd Int. Conf. on Motion and Vibr. Control, pp. 35– 40, 1996.

[65] How Smart Structures Will Work. [Online]. https://science.howstuffworks.com/engineering/structural/smart-structure.htm

[66] J. Bae, D. Inman, W. Belvin H. Sodano, *Improved concept and model of Eddy current damper*.: Journal of Vibration and Acoustics 128, 294–302, 2006.

[67] H. Qi, *Introduction into Finite Element Analysis*.: University of Colorado, 2006.

[68] H. P. Gavinv, *Electrorheological dampers for structural vibration suppression*.: No. 35, University of Michigan, 1994.

[69] H. P. Gavin and R. D. Hanson, *Characterization of an ER active member*.: Structures Congress XII, pp. 863–868, ASCE, 1994.

[70] G. L. Kenaley and M. R. Cutkosky, *Electrorheological fluid-based robotic fingers with tactile sensing*.: Proceedings., 1989 IEEE International Conference on, pp. 132–136, IEEE, 1989.

[71] A. Occhiuzzi, P. Clemente F. Ricciardelli, *Semi-active tuned mass damper control strategy for wind-excited structures*.: Journal of Wind Engineering and Industrial Aerodynamics 88, 2000.

[72] F. Previdi, S. Savaresi, G. Fraternale, N. Gaudiano C. Spelta, *Control of magnetorheological dampers for vibration reduction in a washing machine*.: Mechatronics 19, 410–421, 2009.

[73] C. A. Papadopoulos, *Brakes and clutches using ER fluids*.: Mechatronics, vol. 8, no. 7, pp. 719–726, 1998.

[74] Audi Corporation. Audi magnetic ride. [Online]. https://www.audi-technology-portal.de/en/chassis/suspension-control-systems/audi-magnetic-ride_en

[75] A. S. Shafer and M. R. Kermani, *Development of high performance intrinsically safe 3-dof robot*.: Robotics and Automation (ICRA), 2014 IEEE International Conference, 2014.

[76] A. S. Shafer and M. R. Kermani, *Design and validation of a magneto-rheological clutch for practical control applications in human-friendly manipulation*.: Robotics and Automation (ICRA), 2011 IEEE International Conference on, pp. 4266–4271, IEEE, 2011.

[77] A. S. Shafer and M. R. Kermani, *On the feasibility and suitability of mr fluid clutches in human-friendly manipulators*.: Mechatronics, IEEE/ASME Transactions on, vol. 16, no. 6, pp. 1073–1082, 2011.

[78] 2. P.V. MOHANRAM A.SELVAKUMAR, *ANALYSIS OF ALTERNATIVE COMPOSITE MATERIAL FOR HIGH SPEED PRECISION MACHINE TOOL STRUCTURES*.: DEPARTMENT OF MECHANICAL ENGINEERING, PSG COLLEGE OF TECHNOLOGY, COIMBATORE – 641 004, TAMIL NADU, 2012.

[79] D. Jones, J. Henderson A. Nashif, *Vibration damping*. New York: John Wiley and Sons, 1985.

[80] A.-G. Olabi and A. Grunwald, *Design and application of magneto-rheological fluid*.: Materials & design, vol. 28, no. 10, pp. 2658–2664, 2007.

[81] C. D. Johnson, "Design of Passive Damping Systems.," *ASME. J. Vib. Acoust.*, vol. June, pp. 171-176, 1995.

[82] K.W. Wang M.S. Tsai, "ON THE STRUCTURAL DAMPING CHARACTERISTICS OF ACTIVE PIEZOELECTRIC ACTUATORS WITH PASSIVE SHUNT," *Journal of Sound and Vibration*, vol. 221, no. 1, pp. 1-22, 1999.

[83] L.H. Cadwell, "Magnetic damping: analysis of an eddy current brake using an airtrack," *American Journal of Physics*, vol. 64, no. 7, 1996.

[84] Wouterse J.H., "Critical torque and speed of eddy current brake with widely separated soft iron poles," *IEE Proceedings B (Electric Power Applications*, vol. 138, no. 4, 1991.